Observations of High Definition Symmetric Quasi-Periodic Scintillations in the Mid-Latitude Ionosphere With LOFAR

Trigg, H.; Dorrian, G.; Boyde, B.; Wood, A.; Fallows, R. A.; Mevius, M.

DOI:
10.1029/2023ja032336

JGR Space Physics

RESEARCH ARTICLE
10.1029/2023JA032336

Observations of High Definition Symmetric Quasi-Periodic Scintillations in the Mid-Latitude Ionosphere With LOFAR

H. Trigg[1], G. Dorrian[1], B. Boyde[1], A. Wood[1], R. A. Fallows[2], and M. Mevius[3]

[1]SERENE Group, Electronic, Electrical and Systems Engineering, University of Birmingham, Birmingham, UK, [2]Rutherford Appleton Laboratory, United Kingdom Research and Innovation, Science & Technology Facilities Council, RAL Space, Oxfordshire, UK, [3]ASTRON—The Netherlands Institute for Radio Astronomy, Dwingeloo, The Netherlands

Key Points:

- These are the first reported broadband ionospheric scintillation observations of symmetric quasi-periodic scintillations (QPS)
- The QPS are very highly defined showing the clearest reported examples of ionospheric scintillation arcs in delay-Doppler spectra
- The observations are successfully reproduced using a phase screen model in which plasma density is varied by <1 mTECu

Correspondence to:
G. Dorrian,
g.dorrian@bham.ac.uk

Citation:
Trigg, H., Dorrian, G., Boyde, B., Wood, A., Fallows, R. A., & Mevius, M. (2024). Observations of high definition symmetric quasi-periodic scintillations in the mid-latitude ionosphere with LOFAR. *Journal of Geophysical Research: Space Physics*, *129*, e2023JA032336. https://doi.org/10.1029/2023JA032336

Received 6 DEC 2023
Accepted 18 JUN 2024

Author Contributions:
Formal analysis: H. Trigg
Funding acquisition: G. Dorrian
Investigation: H. Trigg
Methodology: H. Trigg
Software: H. Trigg
Supervision: G. Dorrian
Writing – original draft: G. Dorrian
Writing – review & editing: H. Trigg, G. Dorrian

Abstract We present broadband ionospheric scintillation observations of highly defined symmetric quasi-periodic scintillations (QPS: Maruyama, 1991, https://doi.org/10.1029/91rs00357) caused by plasma structures in the mid-latitude ionosphere using the LOw Frequency ARray (LOFAR: van Haarlem et al., 2013, https://doi.org/10.1051/0004-6361/201220873). Two case studies are shown, one from 15 December 2016, and one from 30 January 2018, in which well-defined main signal fades are observed to be bounded by secondary diffraction fringing. The ionospheric plasma structures effectively behave as a Fresnel obstacle, in which steep plasma gradients at the periphery result in a series of decreasing intensity interference fringes, while the center of the structures largely block the incoming radio signal altogether. In particular, the broadband observing capabilities of LOFAR permit us to see considerable frequency dependent behavior in the QPSs which, to our knowledge, is a new result. We extract some of the clearest examples of scintillation arcs reported in an ionospheric context, from delay-Doppler spectral analysis of these two events. These arcs permit the extraction of propagation velocities for the plasma structures causing the QPSs ranging from 50 to 00 m s^{-1}, depending on the assumed altitude. The spacing between the individual plasma structures ranges between 5 and 20 km. The periodicities of the main signal fades in each event and, in the case of the 2018 data, co-temporal ionosonde data, suggest the propagation of the plasma structures causing the QPSs are in the E-region. Each of the two events is accurately reproduced using a thin screen phase model. Individual signal fades and enhancements were modeled using small variations in total electron content (TEC) amplitudes of order 1 mTECu, demonstrating the sensitivity of LOFAR to very small fluctuations in ionospheric plasma density. To our knowledge these results are among the most detailed observations and modeling of QPSs in the literature.

Plain Language Summary Quasi-periodic scintillations (QPS) are repeated variations in radio signals received on the ground from radio sources beyond the Earth's atmosphere. As these signals pass through plasma structures in the ionosphere they undergo refractive lensing which is seen at the receiver as a distinct signal fade, bounded on both sides by diffraction fringing. Analysis of these QPS using 2D Fourier transforms produced very clear examples of "scintillation arcs" which were used to extract the velocity of the ionospheric plasma producing these patterns. These symmetric quasi-periodic oscillations form a distinct category of radio signals which were reproduced in this study using a phase screen model with very small changes in amplitude, corresponding to variations in ionospheric plasma density along the raypath of <<1% of ionospheric plasma density along the raypath. These features are seen across the wide bandwidth from 24 to 64 MHz, with frequency dependent variation in the width of the signal fade and fringing all being visible. Consequently we see how even these very small changes in ionospheric plasma density are nonetheless able to produce quite distinct variations in received signal strength. The observations in this paper thus demonstrate some of the fundamental physical processes of radio scattering in the ionosphere.

1. Introduction

Ionospheric quasi-periodic scintillations (QPS) are characterized by wave-like recurrent variations in the received power of trans-ionospheric radio signals. In the mid-latitude ionosphere they have been attributed to field-aligned plasma irregularities in sporadic-E layers (Maruyama et al., 2000; Saito et al., 2006; Woodman et al., 1991). The irregularities are extended in altitude over a larger range than typically associated with normal thin sporadic-E layers. Very High Frequency (VHF) radar observations have established altitudes for these structures as high as 130 km, shown that they vary in altitude by up to 30 km as they propagated, and have periodicities comparable

to the local Brunt-Väisälä frequency (Hysell et al., 2014; Yamamoto et al., 1992). When studied with radar, the field aligned plasma irregularities which cause QPS are usually termed quasi-periodic echoes.

Mid-latitude QPS were analyzed by Maruyama (1991) using radio scintillation from geostationary satellite transmissions at 136 MHz and concluded the plasma blob like nature of the irregularities and that they were most likely in the E-region. This study also highlighted that most of the QPS events detected were of the asymmetric kind. Other studies, including Saito et al. (2006) used VHF radar with a central frequency of 46.5 MHz, to characterize the 3-D structure of QP echos as field-aligned elongated plasma structures. Lower latitude QPS studies were made by Patel et al. (2009) using scintillation from satellite transmissions at 250 MHz, who also attributed them to cylindrical shaped ionospheric lenses. Similar cylindrical lens structures were modeled by Davies and Whitehead (1977) used Cornu spirals with plasma densities of $\sim 3 \times 10^{13}$ m^{-3} ($\sim$0.003 TECu), which were in turn used to model signal fading from satellite transmissions and scattering centered at 40 MHz, 140 and 360 MHz, respectively. An earlier study by Elkins and Slack (1969) also recorded QPS in scintillating satellite signals at 137 and 230 MHz Figures 3a and 3b from that paper show examples of Type 1 & 2 QPS.

Yamamoto et al. (1991) categorized their occurrence as "quasi-periodic" or "continuous," with the continuous category being typically observed post-sunrise and manifesting as a series of repeated echo features which persist over several hours. These features were observed to propagate at $\sim$120 m s^{-1}. The quasi-periodic category were, again, caused by plasma structures that were extended in altitude and approximately field-aligned, however only a few of them, or even just one, might be seen in a given observation. Maruyama et al. (2000), modeled altitude-extended complex sporadic-E structures seen in VHF radar echoes as a two-layer E-layer model. The principle argument being that the radio signal variations are a convolution of normal background night time E-layer with a second E-layer, separated in altitude, and containing a relatively dense plasma cloud with high electron density. The plasma cloud had a linear shape and was of approximately 1-km in transverse scale size.

The general form of individual QPSs were categorized into two broad categories by Maruyama (1991, 1995). Type 1 are asymmetric, being characterized by a rapid increase or decrease in received signal power which is then followed by a series of weaker signal oscillations akin to the damped oscillations of a bell after it has been struck. Type 2 are symmetric, in which ringing bell-like signal oscillations both preceded and followed a large signal fade. Indeed, earlier work by Doan and Forsyth (1978) referred to QPS secondary signal oscillations as "ringing irregularities." These secondary signal oscillation features have been attributed to Fresnel diffraction patterns being produced when the radio signal passes through a region of steep plasma density gradient (Bowman, 1989; Maruyama, 1995); the appearance of symmetry or asymmetry thus being an indicator as to whether the causal plasma structures themselves have a symmetric or non-symmetric form as they propagate with differing plasma density gradients on the leading or trailing edges.

Any exo-atmospheric radio source observed from the ground will present a signal that is a convolution of itself and variations imposed upon it during passage through the Earth's ionosphere, usually termed "ionospheric scintillation" (IS). If the source is natural and at astrophysical distances, such as a pulsar or radio galaxy, then scintillation may also be applied to the signal from passage through the interstellar medium and the solar wind. This paper focusses on examples of ionospheric scintillation and, while separating the contributions of these various signatures is not our focus, the interested reader is directed to Fallows et al. (2016). Broadly speaking, ionospheric scintillation observations can be separated from solar wind scintillation on the basis of plasma structure scale size, propagation velocity and direction, and plane-of-sky distance between the Sun and the raypath. Solar wind plasma irregularities detected by interplanetary scintillation can be of order 100,000 km in scale size or larger (e.g., Dorrian et al., 2010), propagate at minimum speeds in excess of 300 kms^{-1} (Breen et al., 1996), and follow an approximately radial outflow direction from the Sun.

The international LOw Frequency ARray (LOFAR: van Haarlem et al., 2013) is an integrated network of ground based broadband radio telescopes operating ostensibly between 10 and 250 MHz. At the time of writing LOFAR consists of 52 ground stations, most of which are located in the Netherlands, however there are also 14 international stations in countries across Europe including, the Republic of Ireland, the UK, Germany, France, Latvia, Sweden, and Poland. In the Netherlands there is a dense cluster of 24 stations geographically co-located which are referred to as the LOFAR "core" stations and given the station ID prefix of CS, such as CS001. Further afield but still within the Netherlands are more stations which are referred to as "remote" stations and given station ID prefixes of RS, such as RS205.

Each LOFAR station consists of two clusters of antennas, the Low Band Antennas (LBA) which operate from 10 to 90 MHz, and the high-band antennas (HBA) which operate from 110 to 250 MHz. Frequencies at the extrema of the nominal LBA and HBA bandwidths are often filtered due to heavy radio frequency interference (RFI), however RFI may still be encountered at other frequencies (e.g., Vruno et al., 2023). In this paper we use data from the LBAs in the UK, Dutch, and Polish stations. The LBAs at each station are a cluster of 96 dual-polarization crossed-dipole antennas; here we use data from the LBAs recorded between 21.8 and 76.1 MHz in 100 channels, with channel spacing optimized for even sampling of wavelength.

As most natural radio sources are broadband emitters and LOFAR is a broadband receiver, we are able to observe scintillation across many frequencies simultaneously. Furthermore, the geographical distribution of LOFAR ground stations throughout Europe lends itself well to tracking the propagation and evolution of ionospheric features in the LOFAR field-of-view. Numerous recent studies have taken advantage of these characteristics to study the mid-latitude ionosphere at relatively unprecedented levels of detail (e.g., Boyde et al., 2022; de Gasperin et al., 2018; Dorrian et al., 2023; Fallows et al., 2020; Mevius et al., 2016).

Ionospheric variations on LOFAR radio signals are generally classed as "diffractive scintillation" if they are generated by plasma structures in the ionosphere that are smaller than the local Fresnel scale (e.g., Fallows et al., 2020). They are characterized by rapid and essentially randomized variations in amplitude, usually across all frequencies, with individual scintilla typically having life times of order ∼10 s. Structures in the ionosphere which are larger than the local Fresnel scale appear with a more periodic and longer lasting signature of up to several minutes (e.g., Boyde et al., 2022). In these cases the ionosphere is behaving more like a large concave lens which undergoes steady deformation as the plasma structure moves through the raypath; the signatures generated in these instances are therefore a consequence of lens-like refraction.

In this paper we present two case studies of LOFAR observations of type 2 QPSs, one in a post-sunset context from 15 December 2016, and another in a post-sunrise context from 30 January 2018, and thus both from approximately solar minimum. Geophysical conditions in both cases were very quiet, with Kp index not exceeding 2+, and F10.7 solar radio flux not exceeding 70. The high frequency resolution and high time resolution capabilities of LOFAR permit a hitherto unprecedented level of detail to be extracted from these phenomena. The first case, from 2016 we refer to as a continuous-type oscillation as we observe 15 individual oscillation events over at least 30-min (the events overlap with the beginning and end of the observing window), with each one having similar characteristics. The second case, from 2018, is seen in full from start to finish and is more quasi-periodic in nature, with six individual oscillation events over an approximately 10-min interval but with particularly clear ringing irregularities visible in each event.

The physics of radio scintillation caused by inhomogeneous plasmas is common to the fields of ionospheric, solar wind, and interstellar scintillation (ISS). Despite the differences in scale and environment, the basic physical processes underlying radio scintillation are the same. Thus it is possible to apply some of the analytical techniques from one field to another. Stinebring et al. (2001) demonstrated the existence of parabolic scintillation arcs in the power spectrum of the intensity of scintillating pulsars. This technique has since been applied in several studies (e.g., Cannon et al., 2006; Fallows et al., 2020) who reported the appearance of the same arc-phenomena in an ionospheric context, and the same technique is applied here in Section 3.2. More recently, Boyde et al. (2024) have used wavelet transforms on radio astronomy calibration data from LOFAR to extract the characteristics of traveling ionospheric disturbances (TID) exhibiting variations in column integrated total electron content of <1 mTECu (1 TECu = 10^{16} e^{-} m^{-2}). The purpose of this paper is to report the observations of an interesting ionospheric phenomena in which some of the clearest examples of scintillation arcs in an ionospheric context yet seen are reported, and to robustly model the data and reproduce the observed scintillation.

The observations are presented in Section 2; in Section 3 we perform some more detailed analysis which takes advantage of the unique broadband observing characteristics of LOFAR which has not been possible with previous observations of QPSs. In Section 4 a brief overview of the model is presented (full details can be found in Boyde et al., 2022), with results from the QPS modeling. To our knowledge the level of detail and the frequency dependent behavior of QPSs seen here is not previously reported and represents the first broadband ionospheric scintillation observations of type 2 QPSs.

2. LOFAR Observations

The data used for this study is from LOFAR observations made of radio sources Cassiopeia-A (Right Ascension: 19h59m28s, Declination: 40.73°) and Cygnus-A (Right Ascension: 23h23m24s, Declination 58.82°) on two separate occasions: 30 January 2018 between 0422 and 0500 UT, and 15 December 2016 between 1818 and 1949 UT (all times hereafter expressed in UT). Cassiopeia-A and Cygnus-A are two of the brightest radio sources in the sky. At 50 MHz Cassiopeia-A and Cygnus-A have flux densities of 27,104 Jy and 22,146 Jy, respectively. They have angular sizes of 7.4 and 2.3 arcminutes. Detailed models of the flux density with angular resolutions of better than 15 arcsec for both sources, using data from the LOFAR LBAs, can be found in de Gasperin et al. (2020).

Samples are taken at a time resolution of 0.01049 s, and the frequency band covers 100 frequency channels between 21.8 and 76.1 MHz. LOFAR station beam sensitivity reduces at lower elevations, and the elevation can change appreciably throughout the observing window. Consequently, a polynomial de-trending function was subtracted from each frequency channel to account for elevation dependencies. To excise RFI, each individual frequency channel was median filtered using a sliding window of 50 data points. Any median filtered data points which exhibited a signal power exceeding 5σ above the standard deviation for that channel were removed. Channels still contaminated heavily with RFI after this process were fully removed and are visible as horizontal white lines in the dynamic spectra. Actual data use was restricted to channels between 22.5 and 64.8 MHz even though data from a slightly wider range was available, as frequencies at the extrema of the available bandwidth were heavily contaminated by RFI. To ease the computational burden of RFI mitigation and elevation dependence on the remaining channels, the data have also been down-sampled in time by a factor of 30, giving a time resolution of ∼0.3 s.

2.1. 30 January 2018

2.1.1. Geophysical Context

Figure 1 shows the geophysical context in the morning of 30 January 2018 between 0000 and 0500. The gray shaded area shows the LOFAR observing window from 0420 to 0500. The Kp index does not exceed 2+ throughout. The auroral electro-jet index (AE: Davis & Sugiura, 1966) is derived from magnetometer data from stations located in the auroral region, and is well established as a standard index for auroral activity. It is based on the field H-component measured at each station and is calculated as the difference between an upper envelope (AU), and a lower envelope (AL) where AE = AU − AL. Sym- and Asy- are the longitudinal symmetric and asymmetric disturbance indices for the H- & D-field components, respectively, and describe field disturbances at mid-latitudes for example, Iyemori (1990).

Figure 2 shows the dynamic spectra of data from LOFAR station PL612, located in Poland (latitude: 53.6°, longitude: 20.6°), from the 30 January 2018 observation of Cygnus-A. Cygnus-A was at an elevation and azimuth of 36.83° and 66.77° respectively, at the beginning of the observation, increasing slightly to 38.30° and 70.64°, respectively, by 0500. The dynamic spectra cover the first 1,590 s of the Cygnus-A observation sliced into three sections of 530 s each. A series of repeating v-shaped signal fades bounded by symmetric signal enhancements are clearly visible and extend from the beginning of the observation at 0422 to at least 0450 with, possibly, fainter examples later on. The features are broader in time at lower frequencies. A key characteristic of the features is their high periodicity, with 15 individual events identified in the first 1,600 s up to 0448. As the phenomenon was ongoing in the field-of-view of the LOFAR station at the start of the observing window, its full extent in time is unknown.

Given the commonality of form shared across all features they have been labeled, with numbered feature four as a reference, as “A,” “B,” and “C.” In the forthcoming text the parts of the features labeled “A” are referred to as “ringing irregularities” or “secondary fringing,” the parts labeled “B” as “boundary signal enhancements,” and “C” as the “v-shaped” or “main” signal fades. The green lines denote the start/end point of each repetition of the periodic feature, as approximated by eye, and are located at the point in the secondary fringing region at which the direction of the frequency-dependent curvature changes from right to left. These positions have been approximated by eye, excluding the region between 600 and 655 s during the transition from events 5 to 6 in which the secondary fringing region is less well-defined, possibly due to the presence of a fainter and less distinct v-shaped fade at ∼630 s.

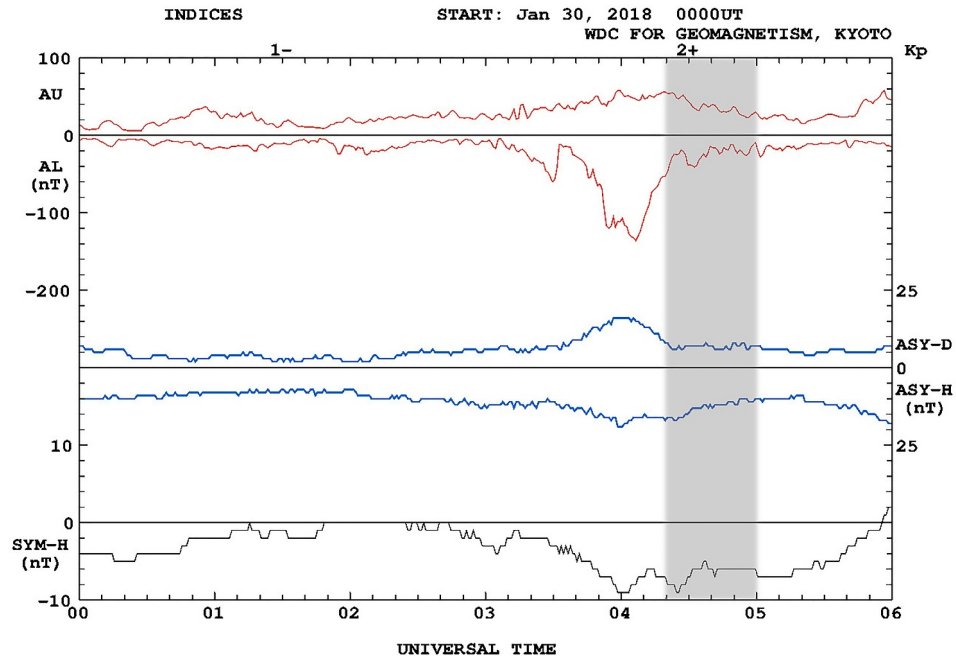

Figure 1. AU/AL auroral indices and ASY-H/D and SYM-H mid-latitude disturbance indices from 0000 to 0600. The LOw Frequency ARray (LOFAR) observation window is shaded in gray. The LOFAR observation window (shaded gray) is immediately preceded by a very modest increases in auroral electrojet activity which is correlated with small perturbations to the mid-latitude ASY-D and ASY-H indices. This activity had declined by the start of the observations however, and had returned to the largely quiet conditions which dominate from 0000 to 0300. The planetary K index (Kp) also remains low throughout, not exceeding 2+.

Figure 2 clearly demonstrates the structure and strong frequency dependence generally present in each feature. Greater fine structure is more visible at lower observing frequencies. The major signal fades in each event are bounded on each side by clear ringing enhancement patterns, with a frequency-dependent curvature. There is also a subtle but repeated asymmetry seen when comparing the boundary signal intensities to the left and right of each numbered main fade, with the left boundary signal having a greater curvature and lower relative intensity. This is observed most prominently in features 12 and 13.

There are other differences between each of the features, and we can generally separate them into three groups. Features 1–4 are the most broad, resulting in less fine structure and fringing, particularly on the leading edge of the major signal fade. Features 5–11 show greater secondary fringing and are generally less broad, with a notable decrease in the relative intensity of the secondary fringing at higher frequencies (seen also in feature 14). Features 11–15 are characterized by distinctly narrower v-shaped fades, less definition in the fringes, and a greater asymmetry with regards to the intensity of the boundary signals on each side of the main signal fade. In some cases the secondary fringes of one event can be seen to overlap those of the next. This particular detail is only visible because these observations are broadband in nature. Analysis of this event with one or a small number of frequency channels, as is typical with many ionospheric scintillation studies relying on GNSS data (e.g., Kintner et al., 2005, 2007; Song et al., 2022), would not have revealed this subtlety.

Figure 3 shows the dynamic spectra of the observation of Cassiopeia-A made over the same time period at station PL612, again with numbered events. Cassiopeia-A was at an azimuth of 24.5° and a moderately low elevation of 28.2° at the start of this observation, rising to 27.6° and 29.8° for elevation and azimuth, respectively, by the end. Similar v-shaped fades and secondary fringing can be seen in the data as those in Figure 2, however in this example we observe less well-defined fringes, and stronger asymmetry in each of the ringing irregularity regions. Once again placing a life time on the event was not possible as it was already ongoing at the beginning of the observing window with fainter v-shaped fades still visible near the end.

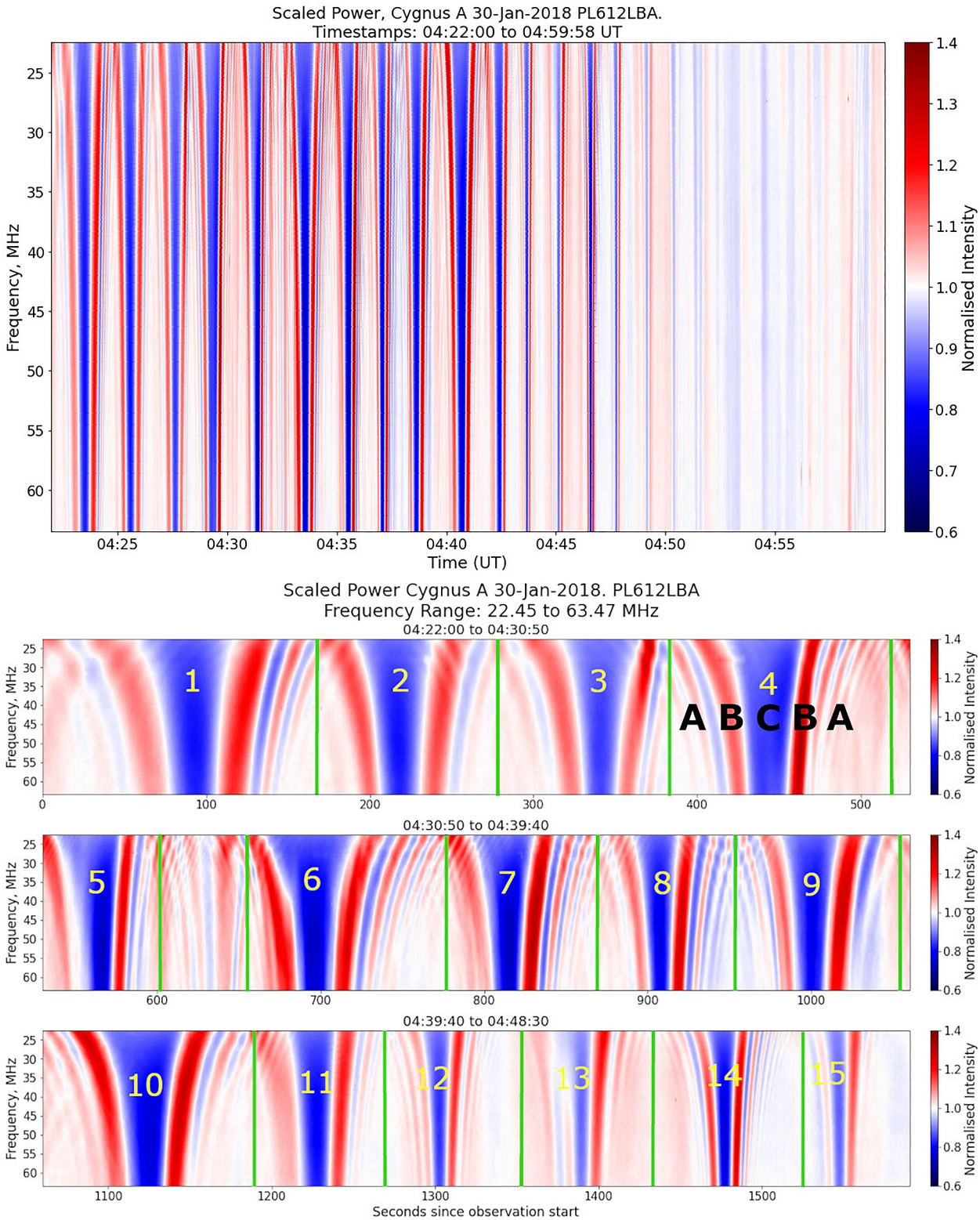

Figure 2. Top panel: Mean-centered dynamic spectra created from filtered data from the 40 min observation of Cygnus-A on 30 January 2018, showing lower frequencies at the top of the plot. Bottom panels: The dynamic spectra with the time axis scaled to better illustrate the fine structure in the features. Each individual feature has been numbered for further discussion. For reference, the regions common to each event labeled A B C we refer to in the text as "secondary fringing/ringing irregularities," "boundary enhancements" or "boundary signals," and "main" or "v-shaped" signal fades, respectively. Signal intensity scales are the same in all plots.

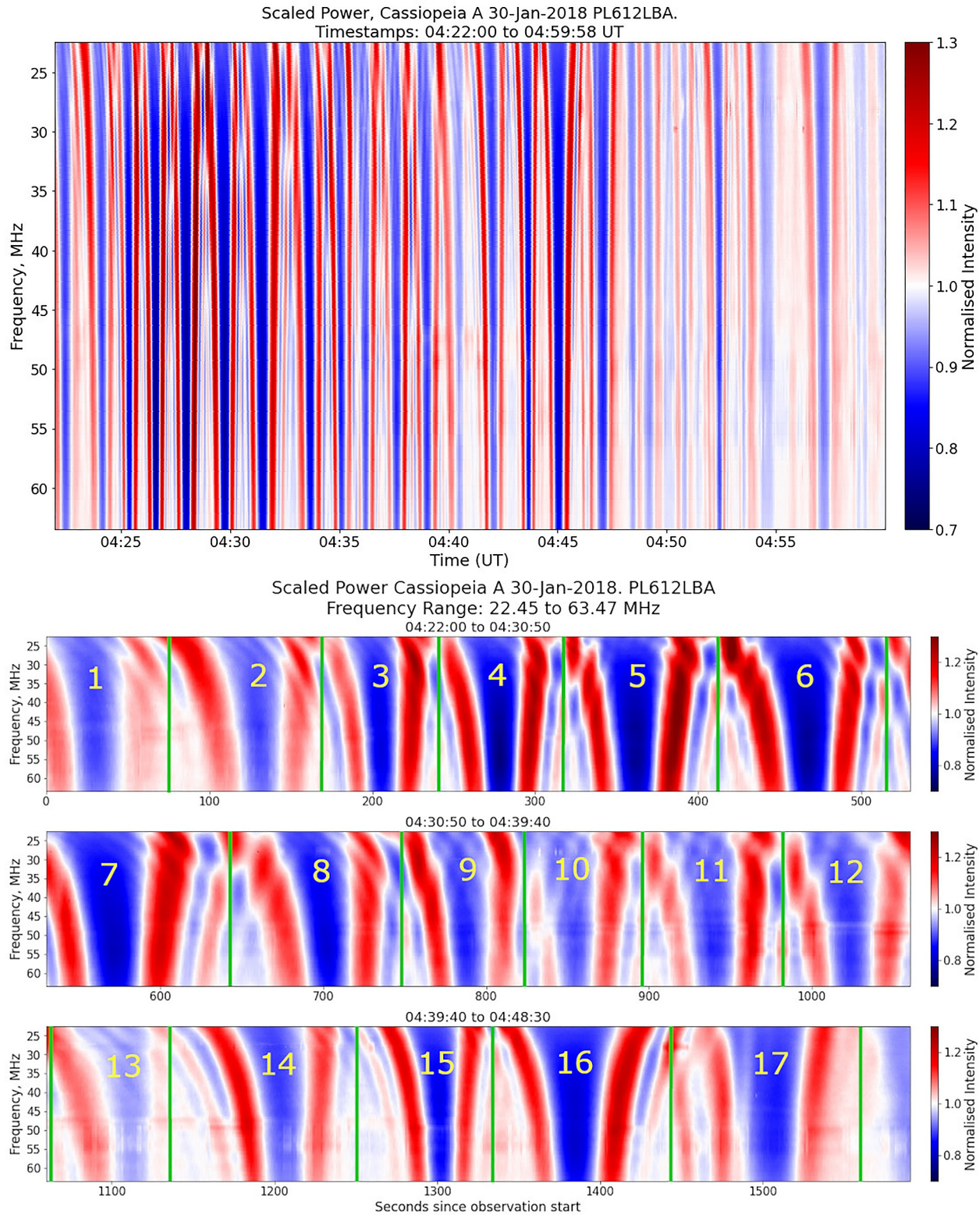

Figure 3. Top panel: Mean-centered dynamic spectra of normalized intensity data from the observation of Cassiopeia-A by station PL612. Bottom panel: Zoomed in features, individually numbered. The bottom three panels are all plotted to the same time scale.

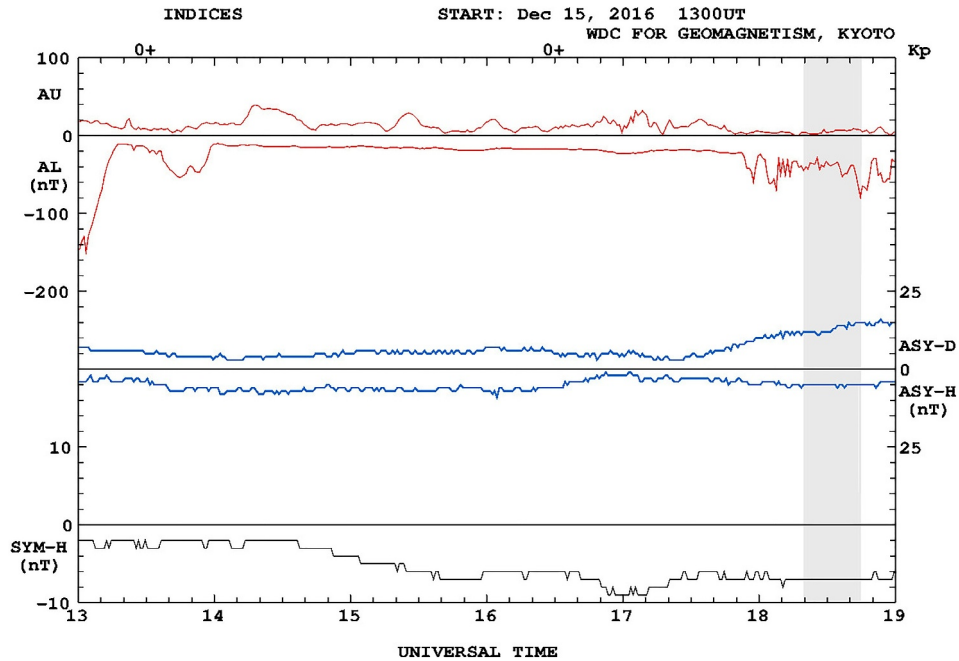

Figure 4. AL & AU auroral indices and ASY-D/H and SYM-H mid-latitude disturbance indices from 1300 to 1900 UT, 15 Dec 2016. The gray shaded area is the LOw Frequency ARray observing window.

The asymmetry is particularly pronounced in events 1 and 13 in which, especially in event 13, the boundary signal enhancement to the right of the main fade is almost invisible. These events also overlap with each other more than they do in the Cygnus-A observations, leading to the ringing enhancements from one event superimposed upon the main fade of the next one. This is especially visible in events 1–2 and 9–13, and at the lower end of the observing frequencies (∼<35 MHz). Estimating event onset time was not possible as v-shaped fades were already present in observation from the beginning.

2.2. 15 December 2016

2.2.1. Geophysical Context

Figure 4 shows the geophysical conditions in the 5-hr prior to the LOFAR observation window (shaded gray). A modest increase in the asymmetry of the D-field component coincides with some small perturbations to the AL index. However, overall auroral conditions were very quiet throughout.

The second set of observations in which similar features appear is from 15 December 2016. As with the previous example, these observations were made using the two sources Cassiopeia-A and Cygnus-A; the dynamic spectrum comes from the LOFAR international station in the UK (UK608: latitude: 51.14°N, longitude: 1.43°W). This observing window ran from 1818 to 1949.

The dynamic spectrum here has been time restricted to approximately the first 20 min of the full 1.5 hr observation period, as no features of interest were visible beyond that time. The bandwidth used here has also been restricted further to 22.5–60.9 MHz due to somewhat heavier RFI contamination at the previously used higher frequencies.

Unlike the 2018 observations using PL612, in this case the v-shaped signal fades with accompanying ringing irregularities were only detected in Cygnus-A observations and were not clearly identifiable in the Cassiopeia-A data, implying a fairly localized plasma scattering region. Data from several of the remote LOFAR stations in the Netherlands also showed evidence of the v-shaped fades however they were less well-defined than for the UK station. At the start of the observing window the elevation and azimuth for Cygnus-A as seen from UK608 was 49.4° and 278.8°, respectively. By the end of the observing window, the elevation of Cygnus-A had decreased to 35.7°, and azimuth had increased to 293.0°.

These observations show similar v-shaped signal fades again bounded on each side by boundary signals and ringing irregularity regions, but with no significant overlap between events and much greater detail of the individual fringes in the ringing irregularity regions being visible. Figure 5 shows the dynamic spectra from UK608 observations of Cygnus-A. We observe similar asymmetric variations as seen in the 2018 data, with the right side fringing of the numbered events significantly more intense. However, the overall form of each event remains highly symmetrical. The ringing irregularity regions, particularly for event 3, are very well defined with >10 individual secondary fringes visible after the main signal fade, and especially at the lower observation frequencies.

3. Data Analysis

We analyze these observations in several stages. First, in Section 3.1, the observation geometry is examined. In Section 3.2, we utilize delay-Doppler spectral analysis to estimate the propagation velocity of each event. Finally in Section 3.3 we examine the periodicities of each case study and attempt to estimate the separation distances between each individual plasma structure based on the estimates for propagation velocity.

3.1. Observing Geometry

To attempt to establish a propagation altitude for each event we examined data from ionosondes located close to ionospheric pierce points (IPP) for the LOFAR stations in each case study. Ionosonde data from FF051 (Fairford, UK, 51.7°N, 1.5°W) and RL052 (Chilton, UK, 51.5°N, 0.6°W) were available for the 2016 observations, but unfortunately suitable data was not available from ionosondes close to the IPP for the 2018 observations. Figure 6 shows four ionograms taken on 15 December 2016, during the 2016 observations. Two are from FF051 at 1815 and 1830 in the left column, and two are from RL052 at 1800 and 1840 in the right column. The ionograms from FF051 have 15-min resolution and the ionograms from RL052 have 10-min resolution.

The two top panels show evidence of semi-blanketing sporadic-E at an altitude of ∼110 km, in which some portion of the radiated energy from the ionosonde passes through the E-layer with sufficient intensity that echoes from the F-layer can also be seen. The F-region traces are still visible in the same frequency range but the backscattered energy appears partially absorbed. The bottom two panels show, aside from what is likely noise at the lowest altitudes, only F-region with the altitude peak of this layer, hmF2, at ∼295 km in both. Sporadic-E seen in the earlier ionograms apparently has dispersed by this time. The F-region traces, now fully visible as a result of the removal of the semi-blanketing E-layer, does shows limited and intermittent frequency spread but lacks any trace bifurcation which might indicate the presence of a traveling ionospheric disturbance in the field-of-view (Bowman et al., 1987; Jiang et al., 2016; Moskaleva & Zaalov, 2013). Furthermore, when the sporadic-E is present, particularly in RL052 (Figure 6, top right panel), it displays altitude spread, indicating that it is not simply a uniform thin ionization layer.

From and Whitehead (1986) investigated several types of E-layer structures and demonstrated that spread-E and semi-blanketing or partially-reflecting sporadic-E is a structured medium consisting of clouds of electrons. By contrast, fully-blanketing or fully reflective sporadic-E is caused by thin sheets of more uniform ionization. The LOFAR observations (Figures 2, 3, and 5) clearly imply structured plasma. Furthermore, the periodicities (see Section 3.3) of the observed features varies between 75 and 125 s, which is much closer to the Brunt-Väisälä frequencies for altitudes of 100–120 km (<5-min) than for F-region altitudes (>10-min; e.g., Borchevkina et al., 2021; Snively & Pasko, 2003). Given the absence of strong evidence for perturbations to the F-region in the ionograms (Figure 6), the events seen in the 2016 data are most likely propagating in the E-region, which, unlike the F-region ionogram traces, clearly shows evidence for structured plasma at two different ionosondes at multiple times throughout the observing window.

We note that the positions of the IPPs at event time in the 2016 data do not exactly overlie the ionosondes. Therefore one should not expect an exact match between structures seen in LOFAR and structures seen in the ionosondes. The picture of the ionosphere they give, in terms of the LOFAR data, is an approximation of overall conditions in the region.

The absence of any such contemporary data from the 2018 observations however means we cannot definitively argue that the 2018 event was located in the E- or F-regions. Instead, we proceed with the analysis for that case on the basis that both possibilities may be true and use the best available estimates for altitude.

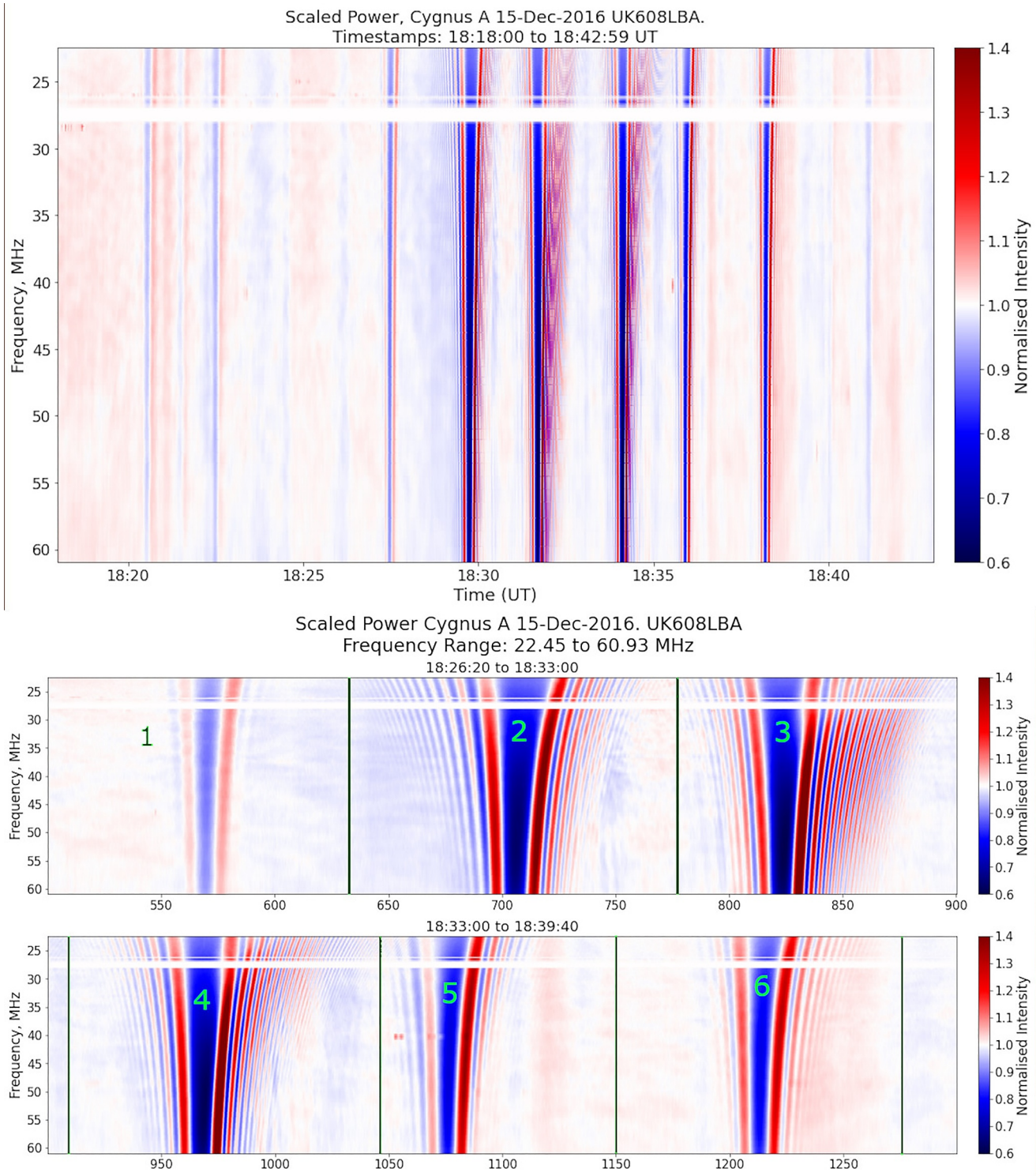

Figure 5. Top panel: Mean-centered dynamic spectrum of the observation of Cygnus-A by LOw Frequency ARray station UK608. Bottom panel: Color scale corresponding to normalized intensity has been capped at a reduced value of 1.4 so that the lower intensity fringing in events 1 and 6 are more visible. All plots use the same intensity scale, and the bottom two panels are plotted to the same time scale. The horizontal white streaks are channels where radio frequency interference which has been removed.

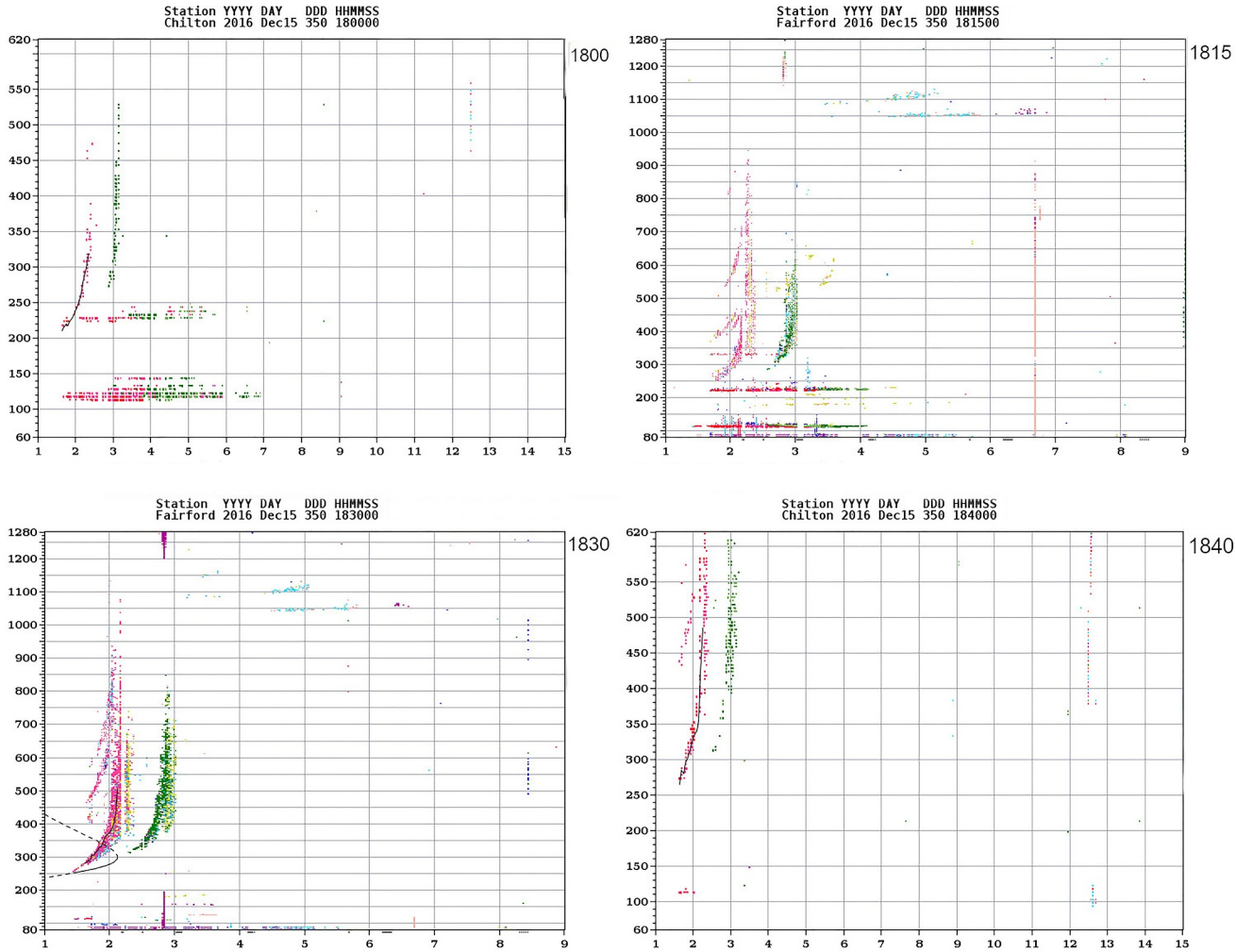

Figure 6. A set of ionograms from the Fairford (left column) and Chilton (right column) ionosondes taken on 15 December 2016 at the times shown, to coincide with the LOw Frequency ARray observations shown in Figure 5. The vertical axis show altitude in km, and the horizontal axis shows frequency (MHz).

Limited and intermittent frequency spread is visible in the F-region, however non-blanketing sporadic-E is also observed in both ionosondes at 1800 on Chilton and 1815 on Fairford. The bottom right panel in particular has a maximum useable frequency of <3 MHz, indicating a particularly low plasma density in the F-region at this time. An estimate was made of the approximate height of both layers using measurements of the average hmE and hmF2 from the Fairford and nearby Chilton ionosondes (located at latitude: 51.70°, longitude: 358.50° and latitude: 51.50°, longitude: 359.40°, respectively). This gives the E-layer peak at 110 km, and the F-layer peak at 297 km.

In Figure 7 IPP maps are shown for the 2016 observations using the UK and remote LOFAR stations. In this case events were only detected in Cygnus-A data; IPP arcs for Cygnus-A are shown in cyan. Even though it seems more likely that the E-region is the appropriate propagation altitude, IPP arcs for 110 and 295 km are presented for comparison. The position of the Fairford ionosonde is also shown. Furthermore, the approximate position and timing of each event as seen on each station is indicated by the yellow spots and accompanying UT timestamps. The IPP projections are calculated using the spherical Earth approximation method described in Section 3 of Dorrian et al. (2023), based on the geometry outlined in Birch et al. (2002). A full set of v-shaped fades consisting of a clear onset and end time set against an undisturbed background ionosphere was seen only from UK608; with partial detections, in which a series of fades were observed to overlap with the beginning or end of the observing window, were seen at several of the remote stations. The IPP arc for LOFAR station RS310LBA is blank to indicate that no QPS were detected by that station. Combined with the fairly rapid appearance and disappearance

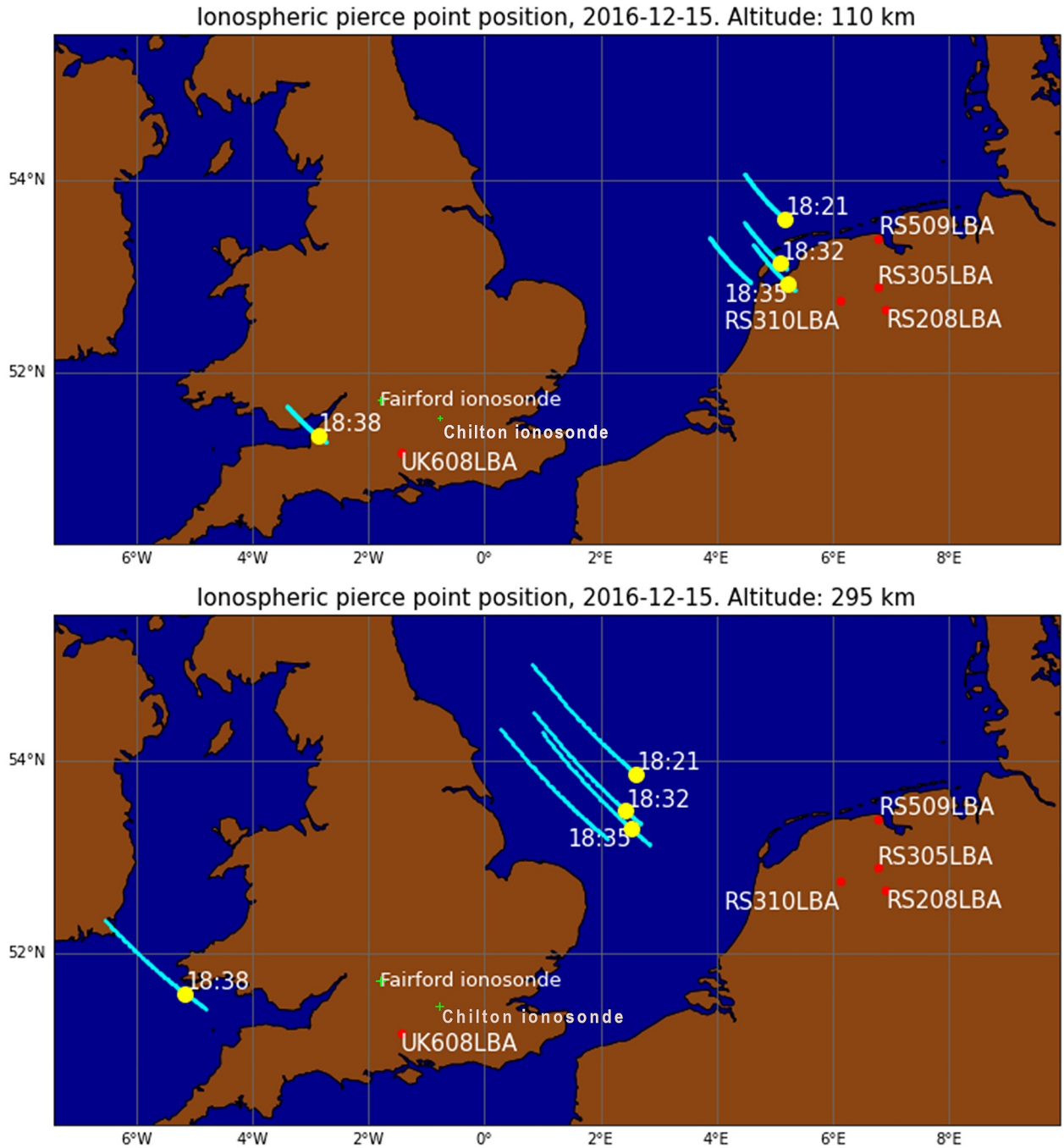

Figure 7. Map of ionospheric pierce point (IPP) location for the 2016 observation of Cygnus-A. Shown on the map is the UK station and several of the remote stations (prefix RS) in the Netherlands in which the event appears. IPP arcs with no event time shown indicate that the event was not seen for that observation, which provides some geographic constraints on the size of the ionospheric feature.

of non-blanketing sporadic-E in the ionograms, this suggests that, rather than some singular feature like a traveling ionospheric disturbance wave passing through the area, there was instead a regional filamentary sporadic-E structure within which multiple QPS generating structures were propagating with similar characteristics.

The absence of useable ionosonde data from the 2018 event restricts the analysis to considering that the propagation was either E- or F-region. It is also highly unlikely to be a D-region phenomena given that the observations were made pre-sunrise in winter when the D-region is typically less prominent (e.g., Renkwitz

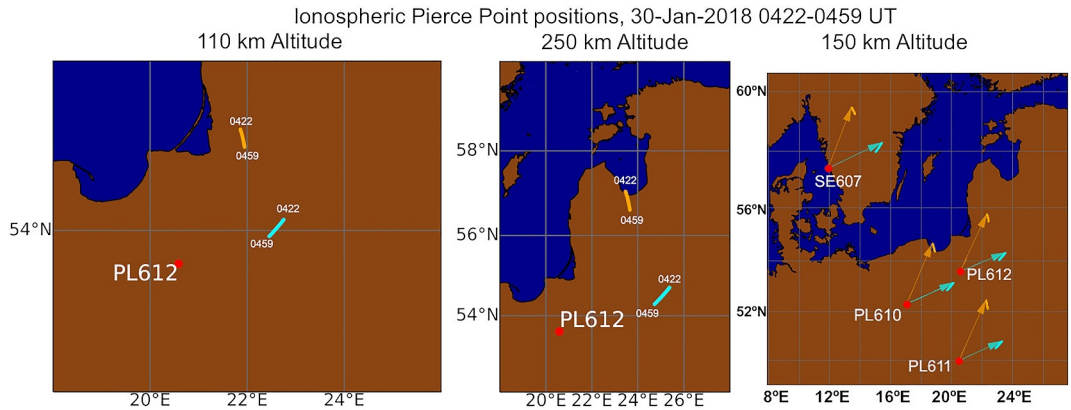

Figure 8. Maps of the position of the ionospheric pierce point (IPP) for the 2018 observations of Cygnus-A (orange arcs) and Cassiopeia-A (cyan arcs). Shown on the left is the estimated location of the IPP for the E-layer at 110 km, in the middle for the F-layer at 250 km, and on the right several nearby LOw Frequency ARray (LOFAR) stations for geographical context. The arrows show the line-of-sight from the respective LOFAR stations to position of the IPP at the start of the observation window.

et al., 2023). As previously mentioned, the geophysical conditions during this observation were very quiet. Consequently we use estimated E- and F-region altitudes from the 2016 International Reference Ionosphere model (IRI: Bilitza et al., 2017) for this area which yielded hmE and hmF2 altitudes of 110 and 250 km respectively. In Figure 8 the left and right panels show the calculated positions of the IPPs for altitudes of 110 and 250 km, respectively, for both Cassiopeia-A (orange arc) and Cygnus-A (cyan arc). The right hand panel shows other LOFAR stations in Poland and Sweden with IPPs projected to 150 km altitude, for geographical context. The start and end times of the observing window are shown as is the position of LOFAR station PL612 which recorded the dynamic spectra shown in Figures 1–3. Because the QPS essentially fills the observing window on both sources we are prevented from assigning any maximum constraints to its total life time. Other than to state that it lasted for a minimum of 37 min (i.e., the length of the observing window). If one assumes, as seems likely, that the events seen on both radio sources are generated by the same overall ionospheric regional structure then, assuming an E-region altitude of 110 km, this regional structure would need to have a horizontal size of at least 115 km to be simultaneously present in the IPP arcs for Cygnus-A and Cassiopeia-A. Likewise, if one assumes an F-region altitude of 250 km, the horizontal size would have to be a minimum of 300 km.

3.2. Delay-Doppler Spectra and Velocity Estimation

The next stage of analysis was the creation of the delay-Doppler spectrum (DDS), from the primary data in the dynamic spectra. The DDS's are the 2-D fast Fourier transforms of windowed sections of the dynamic spectra, and their primary utility here is the determination of propagation velocity. A DDS can exhibit characteristic scintillation arcs (Cordes et al., 2006), the curvature of which is a function both of the propagation velocity of the plasma structures and their distance from the ground station antennas. Hence, if one can isolate either of these characteristics then it is possible to extract the other using Equation 1,

$$L = 2CV^2 \tag{1}$$

where L is distance along the line-of-sight to the scattering region, V is the plane-of-sky velocity component of the moving scattering thin screen, and C is the curvature of the scintillation arc.

Extracting L or V, with the intention of isolating the other, can be accomplished with the use of contemporary data from, for example, ionosondes. Such arcs have been used in the field of ISS for some time (e.g., Stinebring et al., 2001) but, in an ionospheric context, using artificial satellite radio sources first reported by Cannon et al. (2006), and first used on natural radio sources, again in an ionospheric context, with a multi-octave bandwidth, by Fallows et al. (2015).

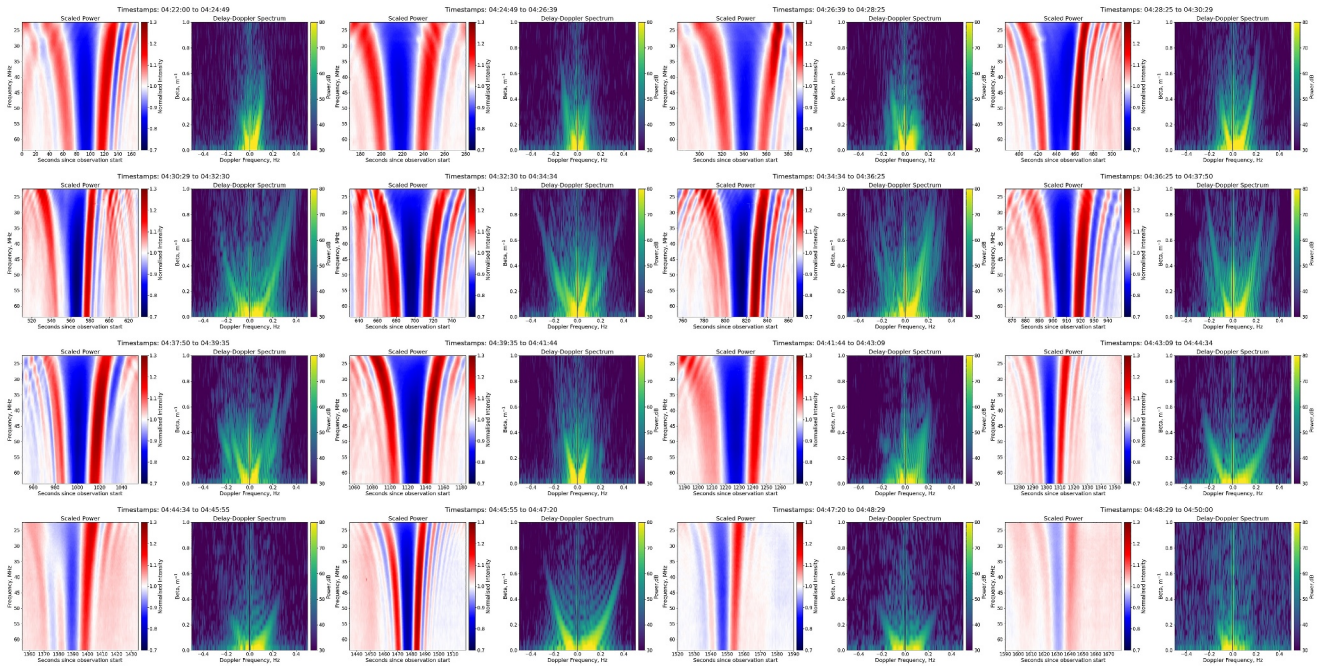

Figure 9. The set of numbered features from Figure 2 (30 January 2018 Cygnus-A dynamic spectra from PL612), alongside their corresponding delay-Doppler spectrum (DDS). Scintillation arcs are clearly visible in all cases and vary considerably during the observation.

The arcs arise partially as a consequence of the Huygens principle in which a plane wave, which is considered as a summation of individual wavelets, is incident upon a scattering screen, in this case ionospheric plasma. An ensemble of secondary spherical wavelets is generated, which undergo mutual interference as they propagate forwards from the screen. Spherical wavelets propagating from the screen at larger distances from the observer will exhibit a greater signal delay time than those which propagate from positions on the screen nearer to the observer, as a result of the longer path lengths they must take. If there is a non-zero relative velocity between the scattering screen and the observer position then the same wavelet ensemble undergoes Doppler shifting, as a function of the observers viewing angle to the scattering screen. The frequency shift is minimized when observing the point on the scattering screen closest to the observer, and increases as the viewing angle increases. The resulting arcs are thus a convolution of both the variable path length taken by each wavelet and the Doppler shift resulting from the relative velocity of the screen with respect to the observer. The vertical axis in each DDS shown here is the Fourier conjugate to the observing wavelength, expressed in units of reciprocal meters (m^{-1}). Multiple arcs appearing in the same DDS are also of interest as different individual arcs imply that there are different populations of scattering plasma in the raypath, and offer a means of separating the velocities of each population. A detailed synopsis of scintillation arc formation can be found in Cordes et al. (2006).

3.2.1. 2018 Data

To isolate the curves from each of the periodic features, the data were sliced into the numbered regions defined in Section 1. Each DDS in Figure 9 was created using the dynamic spectrum from the PL612 observation of Cygnus-A in 2018. The weaker definition of the ringing irregularity regions in the Cassiopeia-A data from this observation precluded the formation of clear arcs. Each sub-plot shows the dynamic spectrum for a single feature in the numbered sequence from Figure 2 and the corresponding DDS. Clear scintillation arcs can be observed in all cases as well as a variation in definition and extent in β.

Parabolas can be fitted to the most well-defined arcs in order to find their curvature, however fitting the curves automatically is technically challenging as any code must understand which data points are part of the arc and which are not, with ambiguities having the potential to significantly affect the curvature estimate (Fallows et al., 2020). Due to the large number of curve fits performed, it was necessary however to utilize an

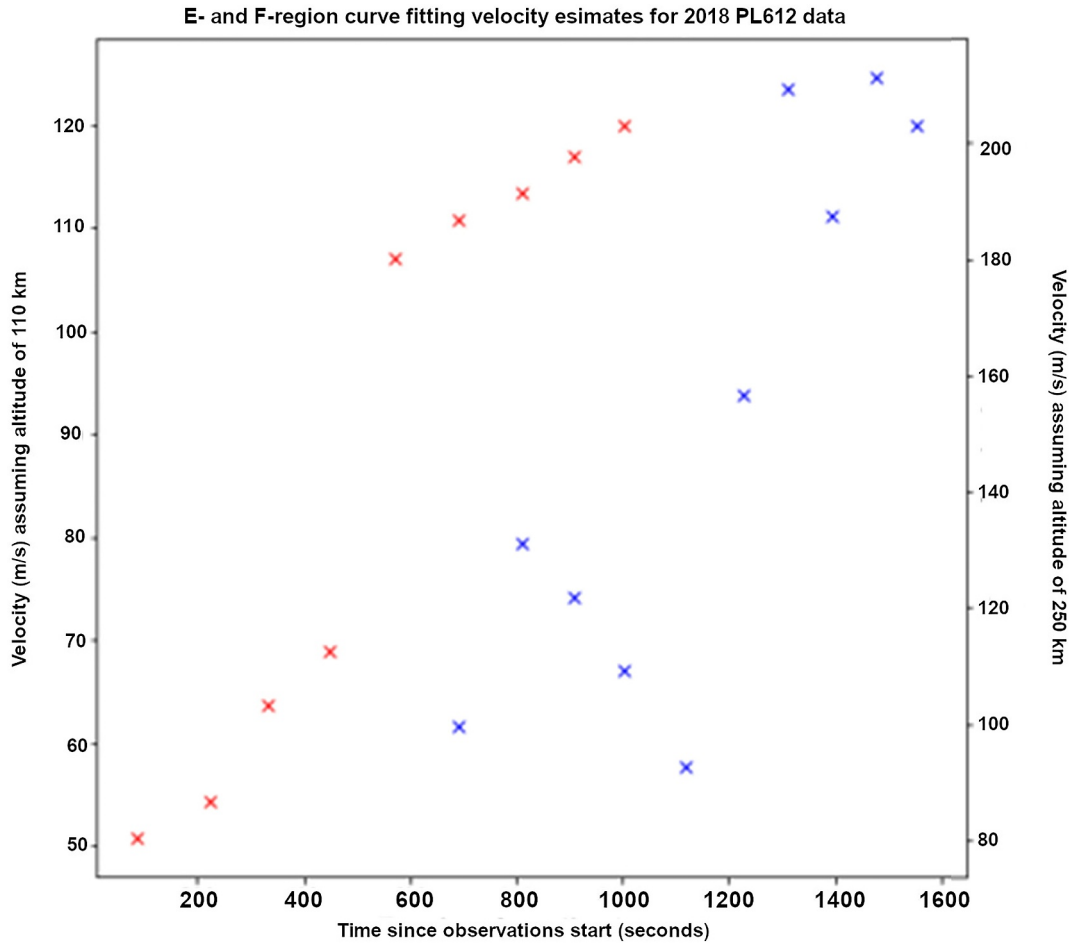

Figure 10. Red crosses denote velocity estimates from primary curve fits, blue crosses denote velocity estimates from secondary curve fits where applicable. The left hand vertical axis shows the velocities if E-region propagation altitude is assumed (110 km), and the right hand vertical axis shows the velocities if F-region propagation altitude is assumed (250 km).

automated routine. Points in the secondary spectrum with a power above a threshold of approximately 60 dB were sampled to isolate the parabolic arc. Arc identification for the code was then simplified by restricting the region of the DDS used for the fit, excluding those regions near the horizontal and vertical axes which are often contaminated by noise. The remaining data points were fitted to a parabola of the form $y = Cx^2 + Bx$ using the least squares method to optimize C and B. While the term in B was used in the fit to account for a shift in the image of the radio signal due to larger scale phase gradients (Cordes et al., 2006), it was not included in the calculation of velocity from curvature.

Moreover, several of the DDS exhibit secondary scintillation arcs which lie closer to the vertical axis than the primary arc. Furthermore, secondary arcs often have a different curvature from the primary arcs. Where clearly identifiable secondary arcs are found, arc curvature has been fitted to these also and, for clarity, velocities extracted in the analysis of these secondary arcs is identified as such. Further complications occasionally arise when the DDS scintillation arcs are asymmetrical, sometimes with the arc being visible only on one side of the central frequency.

The arc fitting process was performed on as many DDS as possible given the limitations on arc definition described above. Furthermore, for each event, two velocity values are extracted, one assuming an E-region propagation altitude and the other assuming an F-region propagation altitude. The results of this process are shown in Figure 10, with red and blue crosses indicating whether the curve fit was performed on a primary arc, or secondary scintillation arc where one was observed. Note, only Cygnus-A observation data

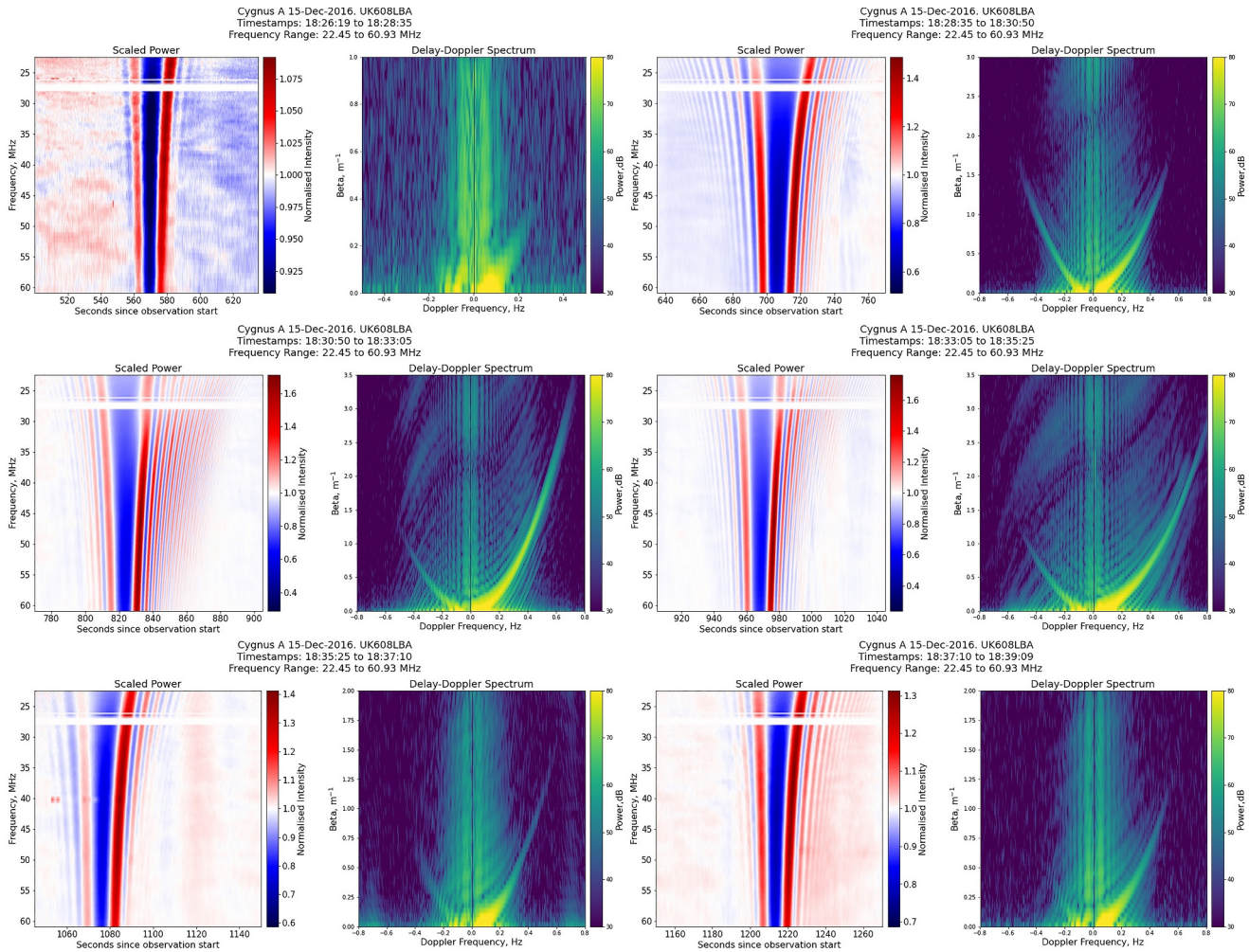

Figure 11. Individual events from the dynamic spectra recorded on UK608, Cygnus-A observations on 15 December 2016, and their corresponding delay-Doppler spectrum (DDS). Asymmetry in the arcs is also a consequence of secondary fringing, but in this case, being due to the clearer definition of fringing.

was used for this process, as the weaker secondary fringing definition in the Cassiopeia-A data suppressed any consistent scintillation arc formation.

A general increase in velocity of approximately 70 m s^{-1}, from 50 to 120 m s^{-1}, is observed when using the E-region altitude scaling. If one uses the F-region scaling then the velocity increase is ∼120 m s^{-1}, rising from 80 to 200 m s^{-1}. If one rearranges Equation 1 for curvature (C) and then assumes that all the plasma structures generating the QPS are all traveling with a constant velocity through the raypath (V), then changes in scintillation arc curvature could only be explained by changes in line-of-sight distance (L) between one v-shaped fade and the next in the sequence. Instances of primary and secondary curves being seen in the same DDS are likely due to more than one population of scattering plasma in the raypath, with each propagating at its own velocity, and both contributing to the overall signal. Once again it is noted that only because these observations are broadband, that such a characteristic may be extracted.

3.2.2. 2016 Data

The same process was then performed on the 2016 data. In Figure 11 the DDS constructed using the 2016 data from UK608 are presented in the same format as Figure 9, with each numbered feature being associated with its corresponding DDS. A combination of the events in the 2016 data being separated in time such that event overlap is minimized and, in several cases, clearer definition of secondary fringing, gives the scintillation arcs in these cases much clearer definition. The sensitivity of arc formation to the presence of well

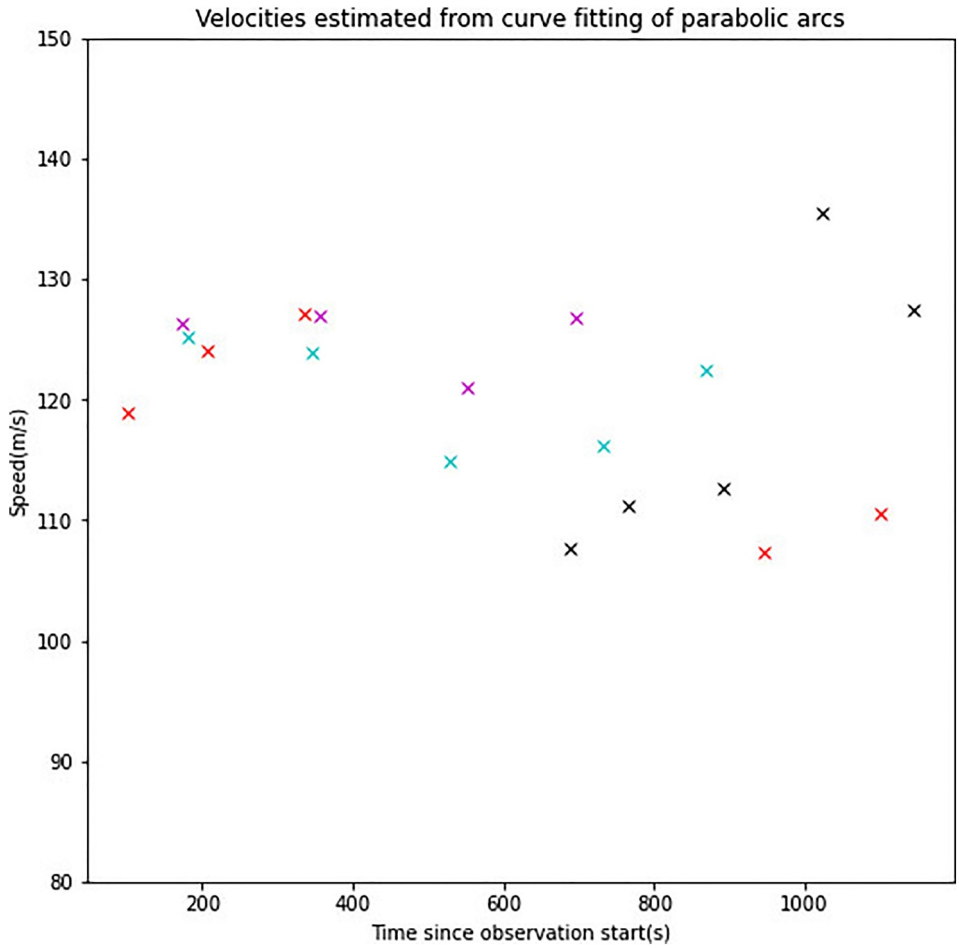

Figure 12. Velocity estimates from curve fitting for the 2016 observations of Cygnus-A using an E-region propagation altitude of 110 km, with different point colors indicating different LOw Frequency ARray stations. Black crosses are for UK608, red for RS208, cyan for RS305, and magenta for RS407. No F-region scaling has been performed in this case given the stronger evidence for event propagation in the E-region.

defined secondary fringing is clearly observed in the lower arc definition in the first panel (top left) in Figure 11 in which the dynamic spectra for that particular event exhibit weak or no fringing, whereas in all the others it is clear. The consistent asymmetry in the arcs throughout is a reflection of the larger number of clearly defined fringes to the right of the main signal fade as well as intensity differences between boundary signals.

Figure 12 shows the results of the velocity analysis using the 2016 data, from all stations in which the QPS is seen. These include the UK station (UK608) and several of the remote stations in the Netherlands (RS208, RS305, RS408), with the different colors indicating different ground stations as shown. Curve fitting for these data was simpler than for the 2018 data as the definition of DDS scintillation arcs was much improved. Additionally, F-region propagation is discounted given the absence of spread-F or trace bifurcation in the ionograms in Figure 6, which would otherwise support perturbations in the F-region. Unlike the analyses of the 2018 data, in this case a consistent propagation velocity range of between 110 and 130 m s^{-1} is seen throughout, with no indication of any plasma screen acceleration.

3.3. Periodograms

With some estimates of propagation velocity now established we can proceed to estimate the separation between sequential v-shaped fades in the scattering screen by investigating their periodicities. To do this,

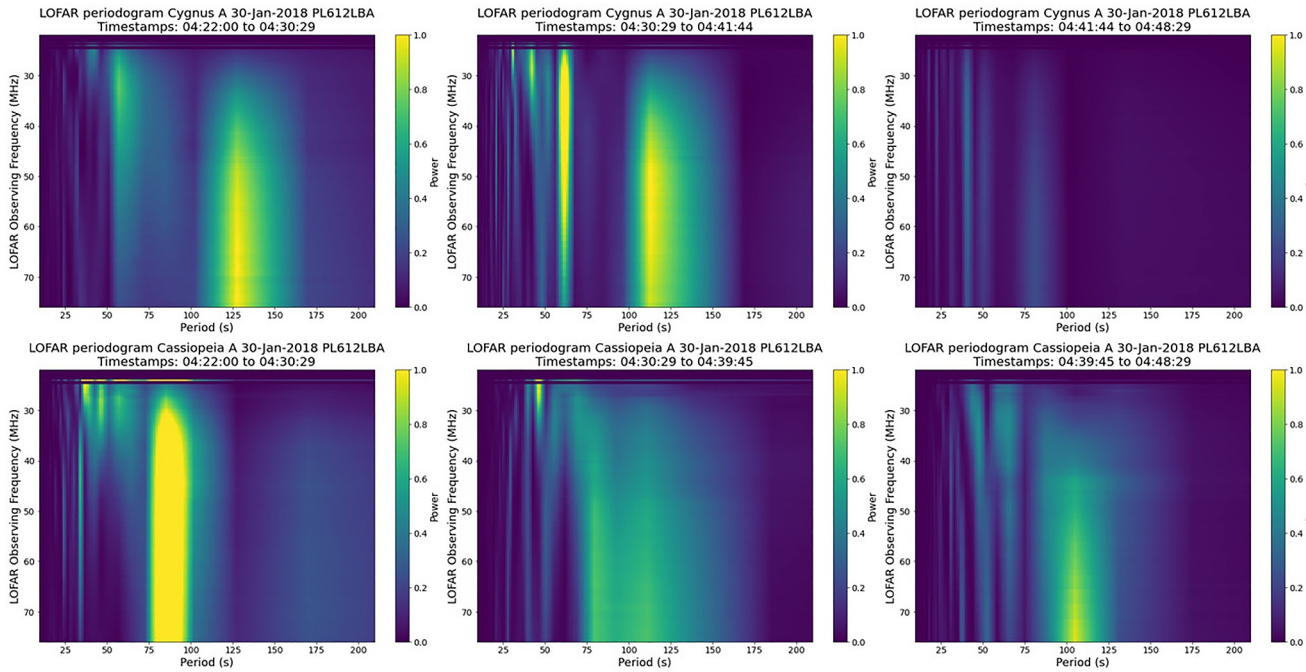

Figure 13. 2D periodograms for Cygnus-A (top row) and Cassiopeia-A (bottom row) observations on 30 January 2018 using LOw Frequency ARray (LOFAR) station PL612, selected for the time windows as shown. Intensity and time scales are the same for all plots.

periodograms were constructed from each frequency channel using Welch's method (Welch, 1967). The periodicities from the 2018 observations using data from PL612 on Cygnus-A are shown in Figure 13 (top row) and Cassiopeia-A (bottom row). The periodograms are taken from time-windowed sections of the dynamic spectra as indicated by the time stamps shown. This was due first to the fact that, in the 2018 observations, a distinct increase in velocity was seen over the course of the observing window. As velocity is a key to extracting distances between each plasma structure, it was therefore important to separate the data into the given sections to avoid smearing out the periodicities. Second, the time lengths of the individual v-shaped fades change throughout the observing window.

The analyzed time sections run from 0422 to 0430 corresponding to events 1–4 in Figure 2, from 0430 to 0441 corresponding to events 5–11, and finally 0441–0448 corresponding to events 12–15. The breaks in each window coincide with broad changes in characteristics of the v-shaped signal fades with 1–4 being quite broad and with somewhat weaker secondary fringing definition. The v-shaped fades 5–11 are consistently of a similar time length and show collectively more secondary fringing. Finally, there is a notable change in width (and hence life time) of the v-shaped fades between events 11 and 12, with events 12 and beyond all having distinctly narrower v-shaped fades. Velocity estimations from 2018 come only from the Cygnus-A observations, however we also present the periodicities from the Cassiopeia-A data for comparison.

Clear peaks in periodicities are observed between 75 and 125 s with several periodicities at shorter time scales. The main broader peaks are the periodicities of the v-shaped signal fades, while the shorter time peaks are caused by the secondary fringing. Peak strength varies throughout the observation window considerably. As shown in Figure 10, the propagation velocity increases substantially during the passage of the event through the raypath, accelerating from ∼50 to ∼120 m s^{-1}, assuming an E-layer altitude, and from ∼80 to 200 m s^{-1}, assuming an F-layer altitude. If these velocities are converted using an average periodicity of 100 s into scale sizes then we are observing spacing between sequential plasma structures of 5–12 km in size assuming an E-region altitude, and 8–20 km if we assume an F-region propagation altitude.

Figure 14 shows the periodicities recorded from the 2016 Cygnus-A data on UK608. Here, given the much shorter event life time and only six discernible individual structures, and the more consistent velocity

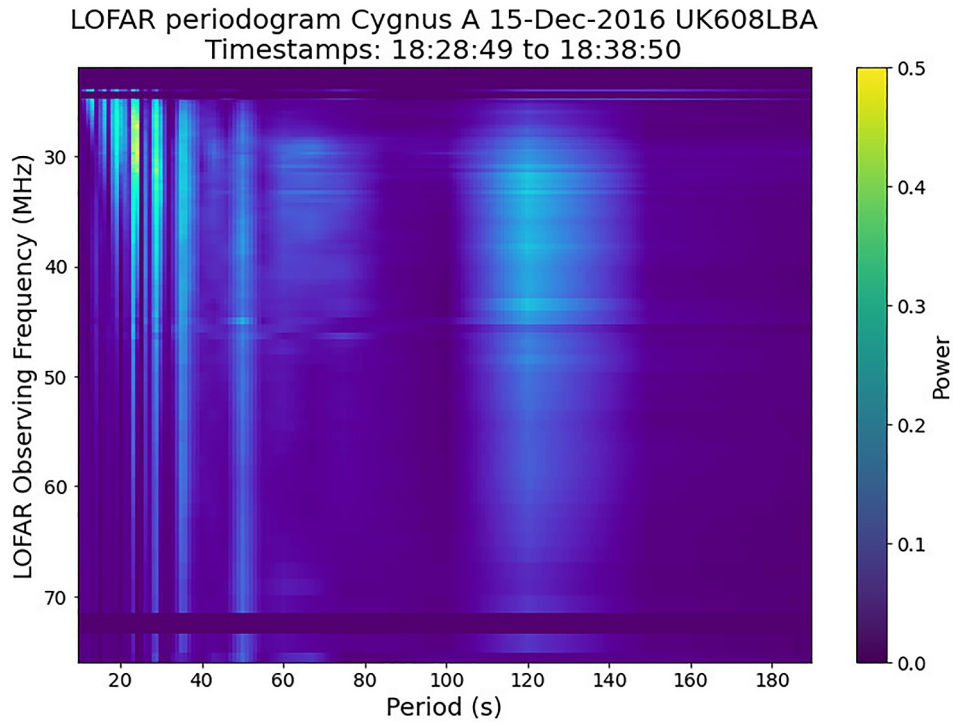

Figure 14. 2D periodogram for observations of Cygnus-A in UK608, 15 December 2016. The main v-shaped fade periodicity peaks at 120 s, with shorter periodicities for the secondary fringing seen at <60 s.

estimation across multiple stations, the periodogram has been calculated over the entire data set without time-windowing. Again a similar pattern is observed, with a main peak in periodicity at ∼120 s, with notable secondary peaks at shorter timescales of 20–50 s. Again, this is due to the main peak being dominated by the main v-shaped signal fades, whilst the shorter periods are from the secondary fringing. Note also, both in Figures 13 and 14, how the frequency dependent behavior of the secondary fringes is reflected in the periodograms, with much clearer periodicity peaks at the lower end of the observing frequency range. Again, this is a characteristic which could only be extracted using broadband observations.

Estimates for velocity from the curve fitting for the 2016 data consistently yielded values of ∼120 m s^{-1}, over several LOFAR stations. If one converts the periodicity peak of ∼120 s, using this velocity, then in this case the individual plasma structures causing the v-shaped fades are separated in distance by ∼14 km. These are approximately the same dimensions as the distance between the primary v-shaped fades in the 2018 case.

4. Modeling

To further assess the characteristics of the plasma structures we have attempted to reproduce them using a Gaussian thin screen phase model of the ionosphere. This approach was recently applied very successfully to spectral caustic lensing features in the ionosphere by Boyde et al. (2022). The model can be tuned with a variety of plasma scattering characteristics such as wave propagation velocity, background plasma density gradient, scattering source size and shape, and altitude (or distance from observer). The main output of a given model run is a synthetic dynamic spectrum which can be compared to the original observation.

The ionosphere is a structure with non-zero thickness, within which lies plasma density irregularities. Hence, any radio wave which transits through the ionosphere will encounter many individual scattering events which induce changes to the signal phase and amplitude. On exiting the ionosphere, the signal will exhibit a phase and amplitude configuration which results from the sum total of all of these scattering events. Consequently, the effects of the full thickness of the ionosphere upon the transiting signal can be approximated as a single thin screen, at a given distance from the observer, in which perturbations to the signal can be modeled as

variations in phase across the screen. The pattern of phase variations can take many forms, such as a sinusoidal wave. Approximating the ionosphere in this way (or as several discrete screens) has been widely used for modeling ionospheric radio propagation (e.g., Briggs & Parkin, 1963; Carrano et al., 2020; Hocke & Igarashi, 2003; Meyer-Vernet, 1980). A schematic, reproduced from Boyde et al. (2022) showing the basis of the phase screen model used here is shown in Figure A1 in the Appendix.

For certain phase screen perturbations, it is possible to derive an analytic solution for the observed intensity distribution as a function of time (e.g., Meyer-Vernet, 1980). However, in most cases a numerical solution is required, the mathematical framework for which is described by Sokolovskiy (2001). The phase screen approach was first applied to replicating LOFAR data by Boyde et al. (2022), building on the earlier theoretical work of Meyer-Vernet (1980). As the solution is derived as a spatial rather than temporal intensity distribution, a constant velocity must be assumed to obtain a dynamic spectrum to compare to observations. The amplitude of the phase perturbation applied by the screen is assumed to be inversely proportional to the radio frequency, which is a valid approximation provided the local plasma frequency remains well below the radio frequency. The ionograms in Figure 6 suggest a peak plasma frequency of ∼3–4 MHz, suggesting that any deviation from this approximation will be negligible except possibly at the lowest observing frequencies.

In the model runs presented here, the source brightness distribution is assumed to be Gaussian and the progression and spacing of the Gaussian ionospheric perturbations as they move through the simulated raypath have been fixed based on the timestamps used to separate the features in Section 2. The amplitude of each Gaussian perturbation (in terms of phase change), and the standard deviation have been adjusted by eye to match the intensity variation, asymmetry, and fringing present in each of the features. The perturbation amplitudes in the model are expressed in rad Hz, and a perturbation of 10^{10} rad Hz corresponds to roughly 1 TECu of line of sight TEC perturbation. The broadening of the v-shaped signal fades, and the density of the secondary fringing is partially a function of the velocity variations described in Section 2. Consequently, modeling of the 2018 data has been split into several sections, bounded by the transition between numbered event characteristics, as explained in Sections 2 and 3. Estimated velocities for each model run were based on the results of the curve fitting excluding the region between features 5 and 6 where no clear numbered event was detected.

Figures 15 and 16 show examples of the results of model reproductions of the original observed features in the LOFAR data from 2018 in PL612. Because of the altitude ambiguity discussed previously, there are two versions of each model run, one using the heights and velocities assuming the event occurs in the F-region, and the other in the E-region. In each plot the top row shows the original LOFAR data, the middle row shows the model runs for the E-region, and the bottom shows the F-region runs.

Figures 17 and 18 show model runs for numbered events 1–6, and 6–12, in the Cassiopeia-A data. Just to note again, that no velocity estimates could be made using curve fitting for the Cassiopeia-A data, however a set of models could still be produced by setting the velocity of each section by eye for a fixed altitude. This is due to the fact that the frequency dependence of the intersection between the secondary fringing of one numbered event and the next is seen clearly and the position of this point is approximately only a function of velocity and spacing, when the altitude is held constant. Once more, this information can only be extracted with broadband observations. In all model plots shown, the timescales for the model runs and the original LOFAR data are identical. The modeling also replicates the less defined secondary fringing in Cassiopeia-A despite changes in amplitudes and scale sizes of the ionospheric perturbations, due to the difference in angular size of the sources.

Despite the simplicity of the model, it is able to accurately replicate the general structure and intensity distribution of the features. It can be seen in Figure 16 how sensitive the model is to velocity; the first v-shaped signal fade is a little too narrow compared to the original whereas the fourth one is a slightly too broad. The model does not accurately replicate some of the asymmetry seen in original signal intensity such as when comparing the intensity and curvature of the left and right side boundary signals (e.g., third feature in Figure 16). It is emphasized that in order to accurately replicate the observed features, modeled TEC perturbations of a few mTECu were necessary, which strongly suggests that the individual v-shaped fades were caused by plasma structures of very small amplitude.

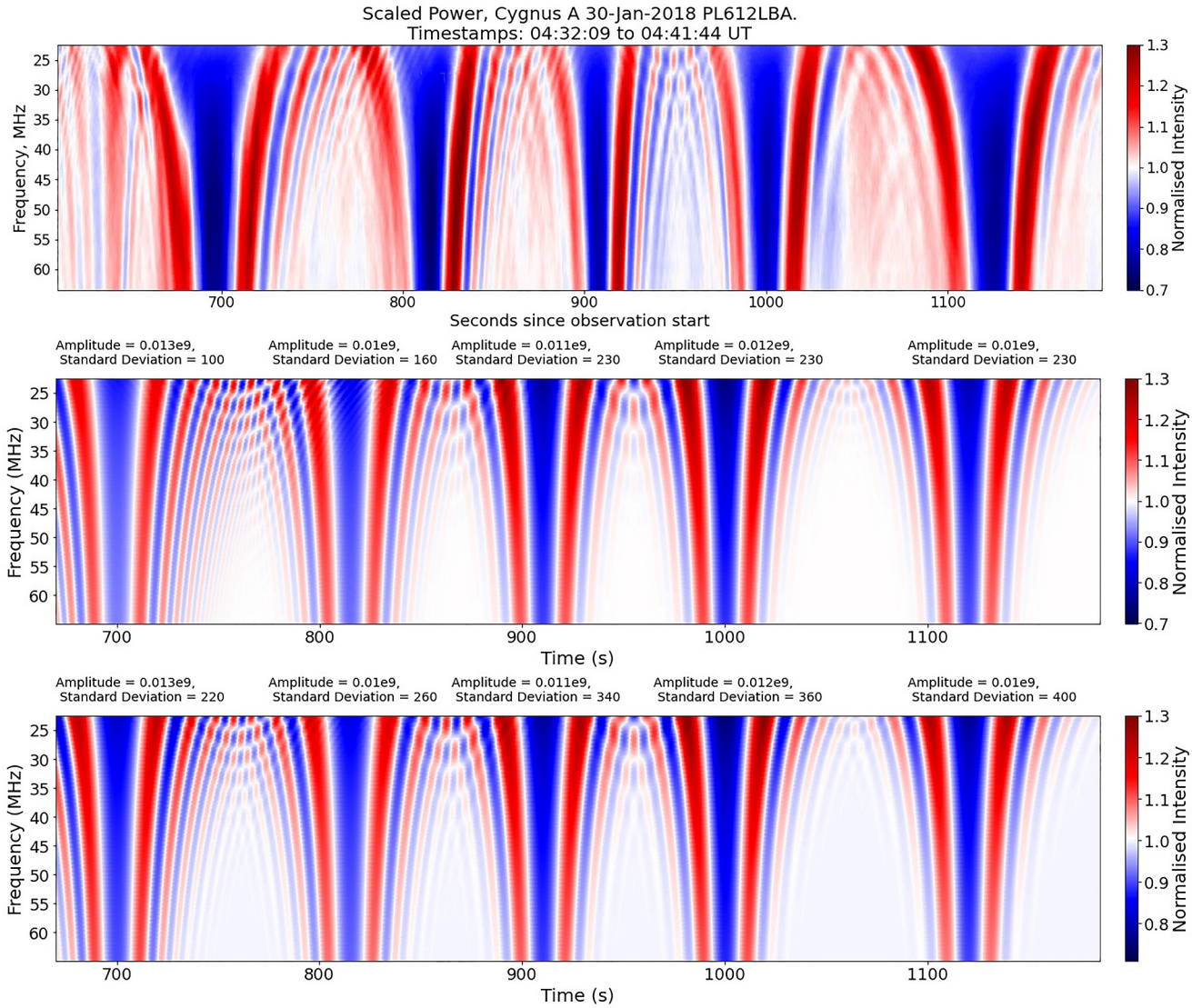

Figure 15. Examples of the output model reproductions, here using numbered features 6–10 in the Cygnus-A data from PL612 on 30 January 2018. Top row: original LOw Frequency ARray dynamic spectra for events 6–10. Middle row: Modeled reproduction of features 6–10, assuming E-region propagation with a velocity of 70 m s^{-1}. Bottom row: Modeled reproduction of features 6–10, assuming F-region propagation with a velocity of 115 m s^{-1}. The values for amplitude and standard deviation define the shape and magnitude of the Gaussian perturbation in each case. The perturbation amplitudes in the model are expressed in rad Hz. A perturbation of 10^{10} rad Hz corresponds to approximately 1 TECu of line of sight total electron content (TEC) perturbation.

In Figure 19 the modeled results for the reproductions of the 2016 observations of Cygnus-A from UK608 are shown. The top panel shows the original LOFAR data and the middle and bottom panels show E- and F-region modeling, respectively. As previously noted, the individual numbered features here are more separated and with extensive secondary fringing regions. Again, the model is well able to reproduce the original LOFAR features; the only differences being subtle asymmetries of the secondary fringing and boundary signal enhancements in a couple of the features. The model also slightly overestimates overall signal intensity; this is possibly a result of an underestimation of sky-noise which affects the original LOFAR signals, particularly at the lower end of the frequency range, but has to be reproduced synthetically in the model. We note that the outputs from the modeling for both 2016 and 2018, while successfully reproducing the original features in the data, are somewhat insensitive to altitude owing to the fact that the scattering characteristics of the features in the original LOFAR data were consistent with a wide range of possible altitudes.

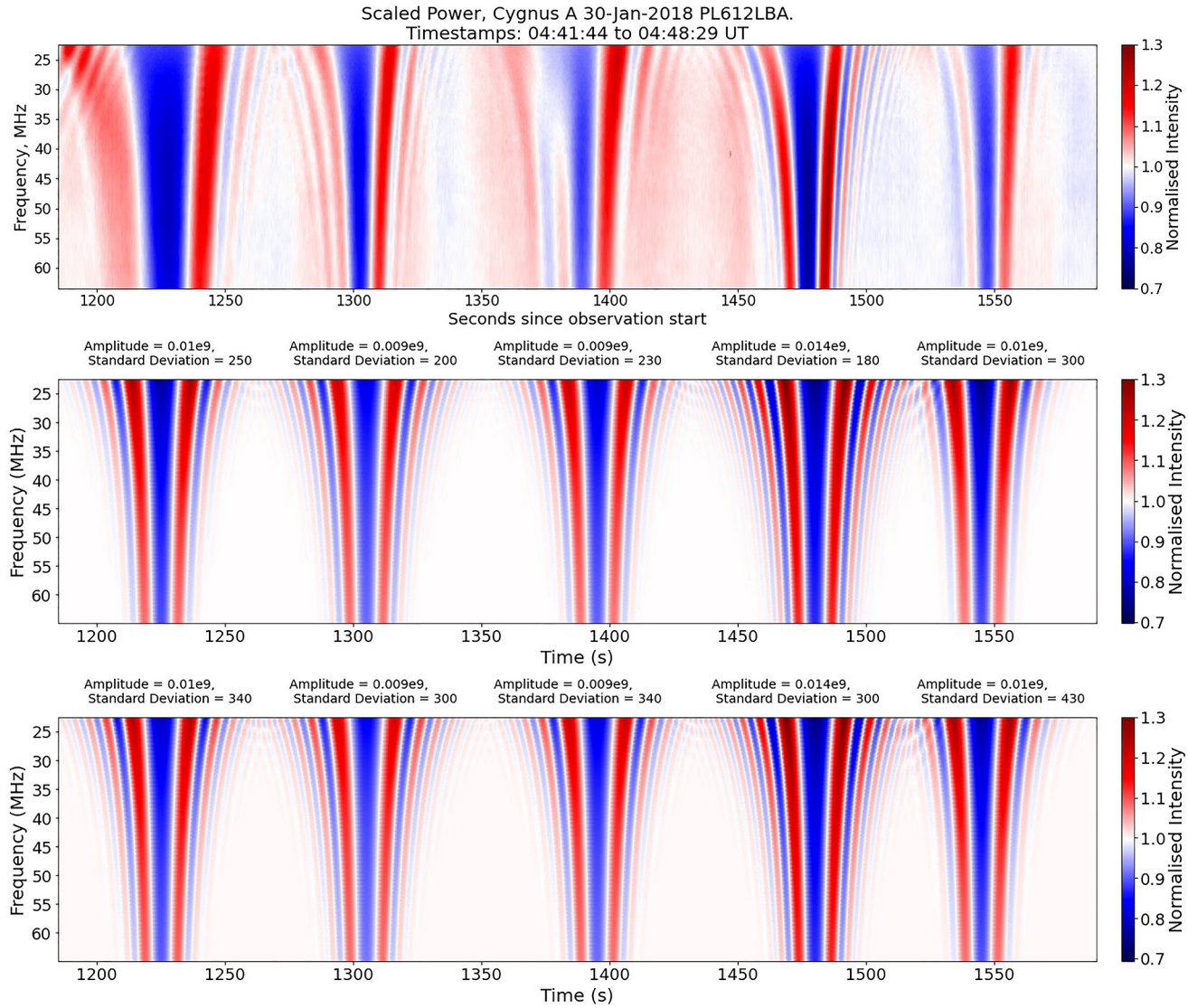

Figure 16. Modeled reproductions of features 11–15 in Cygnus-A data, from LOw Frequency ARray (LOFAR) station PL612 on 30 January 2018. Top row: Original LOFAR data showing numbered events 11–15. Middle row: Modeled reproductions assuming E-region propagation at a velocity of 120 m s^{-1}. Bottom row: Modeled reproductions assuming F-region propagation at 200 m s^{-1}. Intensity scaling is the same in all plots.

5. Discussion

The form of all the features seen in these data and their successful reproductions are all consistent with type 2 QPS in the ionosphere as categorized by Maruyama (1991, 1995). Namely, a distinct signal fade which is symmetrically bounded by large signal enhancements, which we refer to as "boundary signals," and a series of ringing irregularities with varying degrees of definition depending on observing circumstances.

For the 2018 data we are unable to unambiguously determine the altitude of propagation of the QPSs, and so we have proceeded to analyze this event assuming that it maybe propagating either at F- or E-region altitudes, with altitude values having been acquired from the 2016 IRI model. We find propagation velocities, assuming an E-region altitude, starting at 50 m s^{-1} and accelerating throughout the observation to 120 m s^{-1}. If one assumes an F-region propagation then the velocities increase from 80 m s^{-1} at the start to 200 m s^{-1} by the end. Velocity ranges of 50–120 m s^{-1}, consistent with the QPS propagating in the E-region, is within the typical range of expected velocities for a small to medium scale TID, however the wide range is unusual. This definite change in velocity, regardless of altitude, may be caused by different populations of plasma

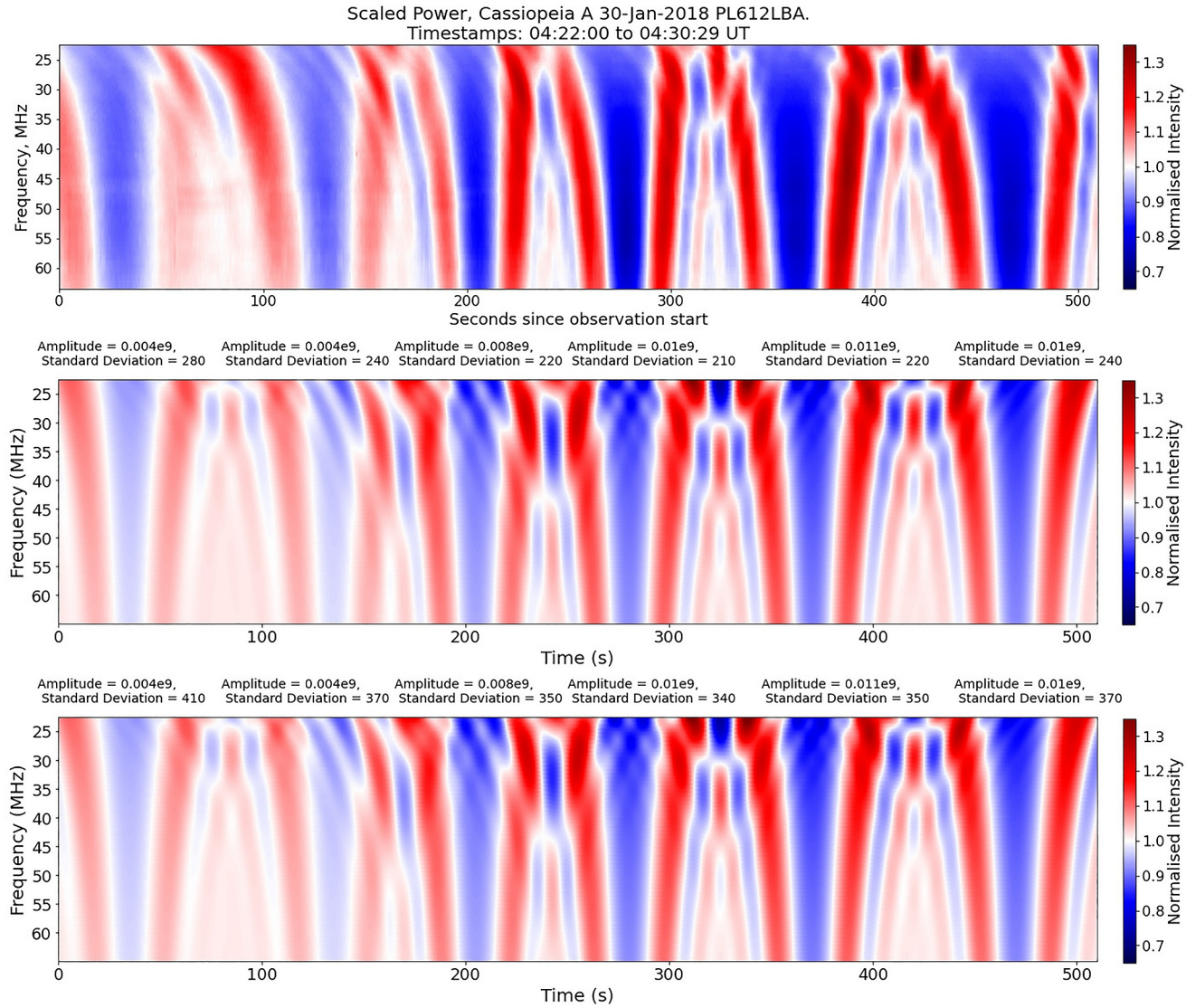

Figure 17. Modeled reproductions of features 1–6 in Cassiopeia-A data, from LOw Frequency ARray (LOFAR) station PL612 on 30 January 2018. Top row: Original LOFAR data showing numbered events 1–6. Middle row: Modeled reproductions assuming E-region propagation at a velocity of 50 m s^{-1}. Bottom row: Modeled reproductions assuming F-region propagation at 80 m s^{-1}. Velocity estimates are made by aligning the position of the cross-over point between the secondary fringing regions of each event, as this is a function of velocity once altitude is held constant.

moving at different altitudes with their own velocities with each dominating the LOFAR signal at different points in the observation. It is noted however that the periodicities of the 2018 data were of order a few minutes which is closer to the Brunt-Väisälä frequency for E-region altitudes than F-region. The large number (>15) of individual signal fades recorded on both radio sources and the fact that this event filled most of the observing window is more consistent with the continuous oscillation type QPSs identified by Yamamoto et al. (1991). It is also noted that Yamamoto et al. (1991) identify continuous oscillations of this kind as being more common in the early morning, which is when the 2018 data were recorded. A continuous oscillation would, in turn, imply some continuous driving processes, although determination of the driving processes behind the events observed are outside the scope of this paper.

For the 2016 study, contemporary data was available from two ionosondes located close to the IPP. The appearance of non-blanketing sporadic-E in the ionograms from these data appearing intermittently throughout the observing window, and the absence of any notable disturbance to the F-region traces make a stronger case for this example of a QPS being located in the E-region. Here the velocity remained more

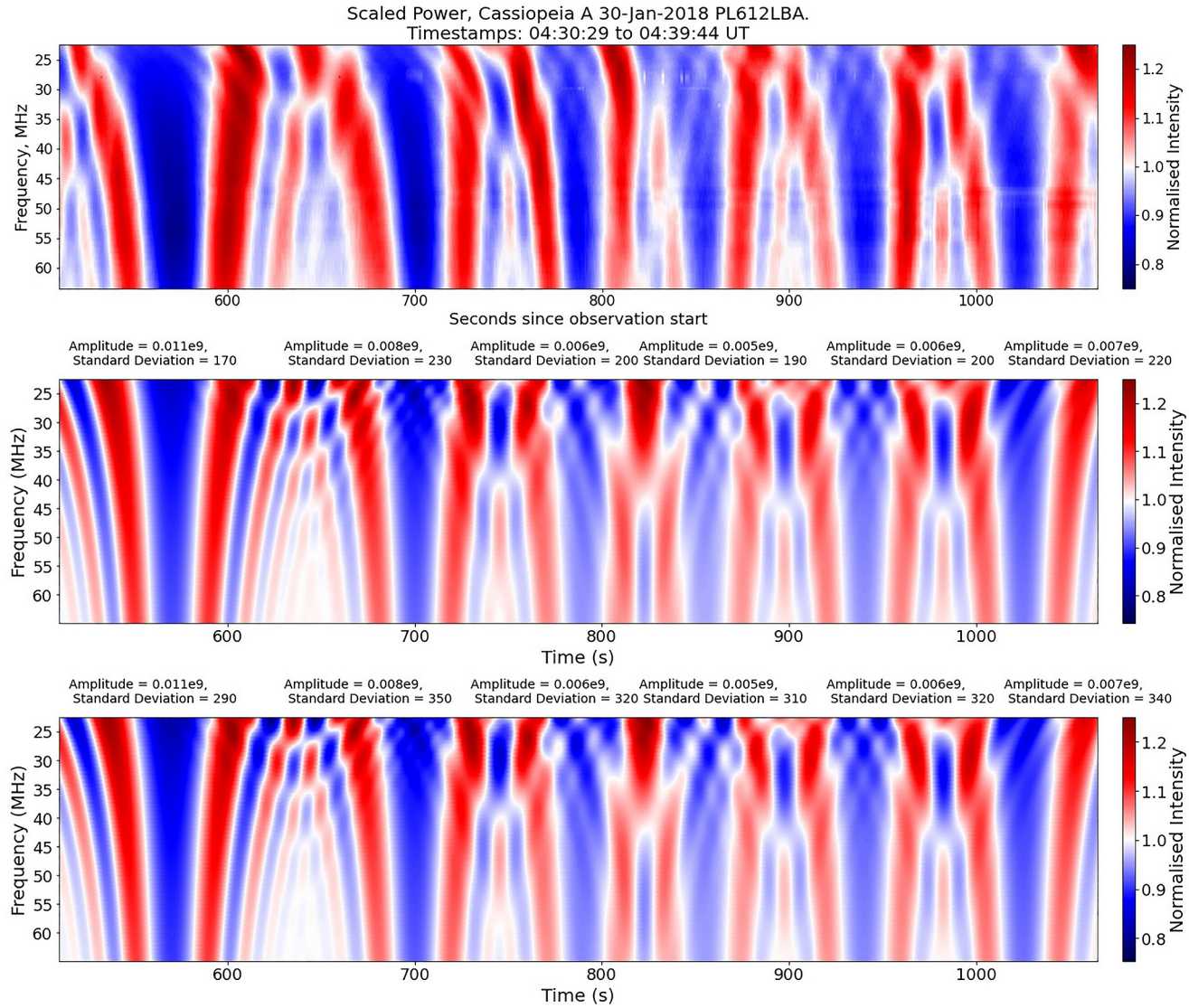

Figure 18. Modeled reproductions of features 6–12 in Cassiopeia-A data, from LOw Frequency ARray (LOFAR) station PL612 on 30 January 2018. Top row: Original LOFAR data showing numbered events 6–12. Middle row: Modeled reproductions assuming E-region propagation at a velocity of 43 m s^{-1}. Bottom row: Modeled reproductions assuming F-region propagation at 70 m s^{-1}. Again, velocities are estimated by the positioning of the cross-over point between the secondary fringes of one event and the next.

constant at ∼120 m s^{-1}, with no strong evidence for acceleration or deceleration. Again, this velocity is reasonably typical of a small to medium scale traveling ionospheric disturbance. However, we could not definitively identify the onset and stop times of this event in most of the LOFAR station which saw it, thus precluding an opportunity to establish in which direction it was propagating. In the IPP maps for this event (Figure 7), there are only a few minutes which seemingly separate the appearance of the QPS in LOFAR stations that are quite widely dispersed, geographically speaking. Therefore it is unlikely that each station saw *exactly* the same event but instead that this QPS was part of some larger regional structure which contained many such examples. This event, consisting of 5–6 individual signal fades, is more consistent with the non-continuous QPS identified by Yamamoto et al. (1991), rather than the continuous type which more accurately defines the 2018 observations.

In the 2018 event, the QPSs were only seen clearly (on both radio sources) from PL612. No other detections were made in other LOFAR stations that were geographically close to PL612. In the 2016 event, the QPSs were detected in a small number of LOFAR stations in Western Europe. Given that, during such

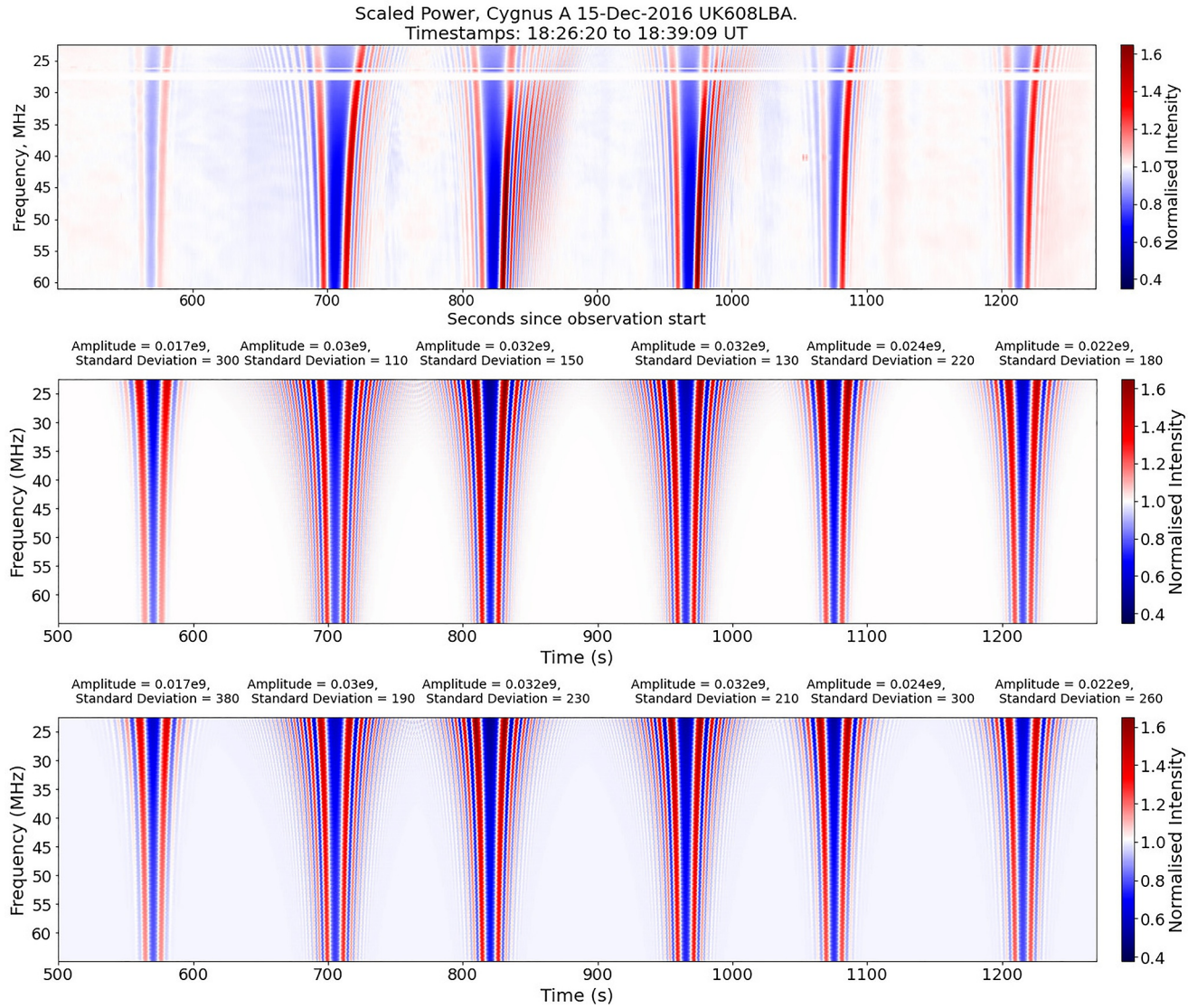

Figure 19. Modeled reproductions of the Cygnus-A data, from LOw Frequency ARray (LOFAR) station UK608 on 15 December 2016. Top panel: Original LOFAR data showing all numbered events. Middle panel: Modeled reproductions assuming E-region propagation at a velocity of 120 m s^{-1}. Bottom panel: Modeled reproductions assuming F-region propagation at 200 m s^{-1}. Velocities are estimated from curve fitting. The model runs and the original data are plotted to the same timescales. Model runs for both E- and F-region altitudes are provided here as the LOFAR data alone could not be used to constrain altitude, as reflected in the modeling output.

observations, LOFAR lines of sight are parallel and have maximum baselines between stations of ∼1,000 km, it is highly unlikely that these QPSs were a feature of the solar wind. Scale sizes of the solar wind irregularities which generate interplanetary scintillation are such that all LOFAR lines-of-sight would likely fall within the spatial extent of the same solar wind feature. That the QPSs are strongly localized geographically therefore makes an ionospheric source far more plausible.

The results of the delay-Doppler spectral analysis of both events have produced some of the clearest examples of scintillation arcs in an ionospheric context. Their definition was such that it was possible to utilize them to estimate the propagation velocity of the QPSs. Furthermore, the presence of primary and secondary arcs in the 2018 observations suggest the presence of two scattering populations of plasma in the ionosphere which would be quite consistent with the two-layer E-layer model proposed by Maruyama et al. (2000).

Considerable characterization and theoretical work on scintillation arcs have been conducted in the closely related field of observations of ISS from pulsars (ISS: e.g., Main et al., 2023; Mall et al., 2022). Vast differences in size and timescales aside, another key consideration in ISS is that the scattering medium may occupy a significant proportion of the raypath. In the ionosphere, the scattering region is much thinner, but also much closer to the observer. However, it has been argued that the appearance of parabolic scintillation arcs in ISS reveal an underlying anisotropy to the scattering medium which is not simply stochastic (Walker et al., 2008). A future development of the present work will be to investigate how observations such as those in this study may inform the field of ISS and vice-versa.

Many of the features observed have been successfully reproduced using a Gaussian phase screen model (Boyde et al., 2022). The model accurately reproduces LOFAR signal intensity across the frequencies used and with similarly clear definition of secondary fringing as the original data. The model is also capable of utilizing a range of source sizes and shapes; the subtle asymmetries seen here may be more accurately reproduced with some form of skewed Gaussian source. We note that, unlike the two-layer sporadic-E model of QPSs proposed by Maruyama et al. (2000), and despite the appearance of primary and secondary arcs in the DDS for the 2018 study, the simpler single phase screen model used here was sufficient to reliably reproduce the QPSs seen in the dynamic spectra. The plasma structures are effectively behaving as simple Fresnel obstacles, in which the center of the structures mostly obscure the radio signal across all frequencies, while steep plasma gradients at the periphery create the series of interference fringes. Recent results by Boyde et al. (2024) demonstrate that LOFAR is readily capable of detecting ionospheric plasma irregularities in the mTEC range.

Whilst the focus of this paper are the QPS themselves, it is worth speculating about their possible driving processes. The 2016 data were acquired on 15 December 2016 between 1826 and 1840 which, when accounting for altitude, is after sunset at the location of the IPP. These data were also acquired under very quiet geophysical conditions (See Section 2.2). Given the small-scale and localized appearance of the QPS, they were likely to be generated from terrestrially generated atmospheric gravity waves (AGW) propagating in the thermosphere. On this date, a high-pressure region was positioned over the UK with very little wind. Skies were clear and it was a calm, dry day with no exceptional weather events (UK Met Office DailyWeather Summary 2016_12). The date of this observation was shortly after the peak in the annual Geminids meteor shower. Given that injection of metallic ions from meteor ablation contributes to ionospheric plasma populations, it is possible that these QPS were in some way related. Meteor plasma trails are known to be thin and flanked with steep plasma density gradients (e.g., Kelley & Ilma, 2016). The trails are known to persist for several seconds and are often located at E-region altitudes (Oppenheim & Dimant, 2006). However, the high periodicity of the QPS is not easily explained by aperiodic plasma injections from meteors. It may be possible to investigate this potential relationship further, but that is beyond the scope of the present study.

The 2018 QPS detected by the Polish LOFAR stations were observed from 0422 to 0500 on 30 January, shortly after a very modest period of geophysical activity in which the Kp-index reached a maximum of 2+ and the lower envelope of the auroral electro-jet index (AL) reached a minimum of −120 nT. Whilst it is possible that this had an influence on the LOFAR observations from this day, we note that, once again, the QPS signatures detected were localized to the lines-of-sight from just one LOFAR station (PL612LBA), and were not seen elsewhere. This implies that the plasma structures generating the QPS are likewise localized in nature rather than exhibiting the characteristics of a larger scale TID more characteristic of having been caused by geomagnetic substorms at high latitude (Hunsucker, 1982). Hence, as with the 2016 data, these events may have been driven by localized and terrestrially generated AGW. The proximity of the IPP to the solar terminator may also be significant though again one might expect a sunrise-generated set of propagating AGW to be observable as TIDs over a wider region. Finally, the 2018 data were collected immediately prior to the Winter 2018 Sudden Stratospheric Warming event (Rao et al., 2018). It is possible that disturbances to the high latitude stratospheric jet stream during this time may have played a role in generating the QPS.

This study presents the first broadband observations of symmetric QPS, characterized by a deep broadband signal fade, flanked by ringing irregularity patterns. The QPS are sufficiently well-defined in LOFAR dynamic spectra that particularly clear examples of scintillation arcs could be extracted from these observations using delay-Doppler spectral analysis. The curvature of these arcs have been used to calculate the propagation velocity of the plasma irregularities. In the 2018 case study the velocities were calculated based on the assumed altitude of the

E- and F-region ionospheres, estimated from the IRI 2016 model, as accelerating from 50 to 120 m s^{-1}, assuming an E-region altitude or 80–200 m s^{-1}, assuming an F-region altitude. In the 2016 case study the velocities were more constant at ∼120 m s^{-1}. In this case study the altitude was estimated from cotemporal ionograms which showed sporadic-E in the area. Two dimensional periodograms, coupled with the calculated velocities from the scintillation arcs, have enable the spacing between the individual plasma structures which generate the QPS to be estimated as between 5 and 12 km for an E-region altitude or 8–20 km for an F-region altitude. The LOFAR dynamic spectra have been successfully modeled using a variation of the thin phase screen model outlined in Boyde et al. (2022) and demonstrate that the plasma irregularities were of very small amplitude, of order 1 mTECu.

6. Conclusions

Broadband trans-ionospheric radio propagation observations of highly-defined symmetric QPS have been made in two case studies, with the International LOFAR Telescope. These oscillations are characterized by a distinct broadband signal fade which is approximately v-shaped when observed in dynamic spectra across the frequency range 22.5–64.8 MHz. The v-shaped fades are bounded on both sides by a series of secondary diffraction fringes. The diffraction fringes are more distinct and with greater spread at the lower frequencies. The first case study, from January 2018, was of a continuous series of such oscillations which persisted in the raypath for the full duration of the 90-min observing window. The second from data taken in December 2016 was of shorter duration with just 6 v-shaped fades, but with particularly well-defined secondary diffraction fringing. These features yielded very clear scintillation arcs in their corresponding delay-Doppler spectra, and were successfully modeled using a Gaussian thin-screen phase model, with amplitudes of <mTECu. They constitute some of the clearest examples of these features thus far reported, and are the first to be observed in broadband.

Appendix A: Phase Screen Model

Figure A1 shows the thin phase screen used here to replicate the QPS observed in the LOFAR dynamic spectra. The observed phase of the incoming wave (Φ), at a given frequency (f), is modulated as a function of distance along the screen (x). The perturbation propagates along the screen as a sequence of Gaussians at velocity v, each with their own amplitude Φ_0, standard deviation Δx and separated by a variable distance L from the neighboring Gaussian.

The phase perturbation observable at X is given by Equation A1:

$$\Phi(x,t) = \sum_{i=0}^{n} \frac{\Phi_{0i}}{f} \exp\left(\frac{(x - x_i - vt)^2}{2\Delta x_i^2}\right) \tag{A1}$$

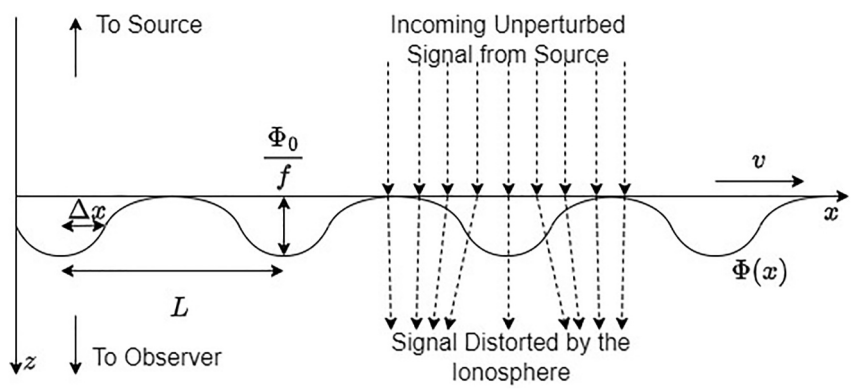

Figure A1. The configuration of the thin-phase scattering screen used in this study as the basis for modeling the ionospheric scattering which produced the Quasi-periodic scintillations.

where Φ_0 is the phase change imposed by the screen at a distance from the screen of $z = 0$ and time t, and where α represents the phase gradient of the background ionosphere upon which the screen perturbations are imposed. For further details the interested reader is directed to Boyde et al. (2022) and Meyer-Vernet (1980).

Data Availability Statement

The LOFAR data for these observations can be accessed from the LOFAR Long Term Archive (LTA: https://lta.lofar.eu), under the project code LC9_001 with observation ID L640829 for the 2018 case study, and under LC7_001 with observation ID L562627 for the 2016 case study. The ionosonde data were accessed through the Global Ionospheric Radio Observatory, accessible at http://hpde.io/SMWG/Observatory/GIRO. The AU, AL, Asy-D, Asy-H, Sym-H & Kp indices used in this paper were provided by the WDC for Geomagnetism, Kyoto (http://wdc.kugi.kyoto-u.ac.jp/wdc/Sec3.html).

Acknowledgments
The International LOFAR Telescope is designed and constructed by ASTRON. It has observing, data processing, and data storage facilities in several countries that are owned by various parties (each with their own funding sources) and that are collectively operated by the ILT foundation under a joint scientific policy. The ILT resources have benefited from the following recent major funding sources: CNRS-INSU, Observatoire de Paris and Université d'Orléans, France; BMBF, MIWF-NRW, MPG, Germany; Science Foundation Ireland (SFI), Department of Business, Enterprise and Innovation (DBEI), Ireland; NWO, The Netherlands; The Science and Technology Facilities Council, UK; Ministry of Science and Higher Education, Poland. H. Trigg was funded for this work by a student summer bursary grant from the Royal Astronomical Society (PI: G. Dorrian). This work is supported by the Leverhulme Trust under Research Project Grant RPG-2020-140. Ben Boyde acknowledges receipt of a PhD studentship from the same grant. R. A. Fallows was partially supported by the LOFAR4SW project, funded by the European Community's Horizon 2020 Program H2020 INFRADEV-2017-1 under Grant 777442.

References

Bilitza, D., Altadill, D., Truhlik, V., Shubin, V., Galkin, I., Reinisch, B., & Huang, X. (2017). International Reference Ionosphere 2016: From ionospheric climate to real-time weather predictions. *Space Weather*, *15*(2), 418–429. https://doi.org/10.1002/2016SW001593

Birch, M. J., Hargreaves, J. K., & Bailey, G. J. (2002). On the use of an effective ionospheric height in electron content measurement by GPS reception. *Radio Science*, *37*(1), 15-1–15-19. https://doi.org/10.1029/2000RS002601

Borchevkina, O. P., Adamson, S. O., Dyakov, Y. A., Karpov, I. V., Golubkov, G. V., Wang, P.-K., & Golubkov, M. G. (2021). The influence of tropospheric processes on disturbances in the D and E ionospheric layers. *Atmosphere*, *12*(9), 1116. https://doi.org/10.3390/atmos12091116

Bowman, G. G. (1989). Quasi-periodic scintillations at mid-latitudes and their possible association with ionospheric sporadic-E structures. *Annales Geophysicae*, *7*, 259–267. ISSN 0980-8752. Retrieved from https://ui.adsabs.harvard.edu/abs/1989AnGeo…7…259B

Bowman, G. G., Dunne, G. S., & Hainsworth, D. W. (1987). Mid-latitude spread-F occurrence during daylight hours. *Journal of Atmospheric and Terrestrial Physics*, *49*(2), 165–176. https://doi.org/10.1016/0021-9169(87)90051-1

Boyde, B., Wood, A., Dorrian, G., Fallows, R. A., Themens, D., Mielich, J., et al. (2022). Lensing from small-scale travelling ionospheric disturbances observed using LOFAR. *Journal of Space Weather and Space Climate*, *12*, 34. https://doi.org/10.1051/swsc/2022030

Boyde, B., Wood, A., Dorrian, G., Sweijen, F., de Gasperin, F., Mevius, M., et al. (2024). Wavelet analysis of differential TEC measurements obtained using LOFAR. *Radio Science*, *59*(4), e2023RS007871. https://doi.org/10.1029/023RS007871

Breen, A. R., Coles, W. A., Grall, R. R., Klinglesmith, M. T., Markkanen, J., Moran, P. J., et al. (1996). EISCAT measurements of the solar wind. *Annales Geophysicae*, *14*(12), 1235–1245. https://doi.org/10.1007/s00585-996-1235-8

Briggs, B. H., & Parkin, I. A. (1963). On the variation of radio star and satellite scintillations with zenith angle. *Journal of Atmospheric and Terrestrial Physics*, *25*(6), 339–366. https://doi.org/10.1016/0021-9169(63)90150-8

Cannon, P. S., Groves, K., Fraser, D. J., Donnelly, W. J., & Perrier, K. (2006). Signal distortion on VHF/UHF transionospheric paths: First results from the Wideband Ionospheric Distortion Experiment. *Radio Science*, *41*(5), RS5S40. https://doi.org/10.1029/2005RS003369

Carrano, C. S., Retterer, J. M., Groves, K. M., Crowley, G., Duly, T. M., & Hunton, D. E. (2020). Wave-optics analysis of HF propagation through traveling ionospheric disturbances and developing plasma bubbles. In *2020 XXXIIIrd General Assembly and Scientific Symposium of the International Union of Radio Science*. IEEE. https://doi.org/10.23919/URSIGASS49373.2020.9232348

Cordes, J. M., Rickett, B. J., Stinebring, D. R., & Coles, W. A. (2006). Theory of parabolic arcs in interstellar scintillation spectra. *The Astrophysical Journal*, *637*(1), 346–365. https://doi.org/10.1086/498332

Davies, K., & Whitehead, J. D. (1977). A radio lens in the ionosphere. *Journal of Atmospheric and Terrestrial Physics*, *39*(3), 383–387. https://doi.org/10.1016/S0021-9169(77)90153-2

Davis, T. N., & Sugiura, M. (1966). Auroral electrojet activity index AE and its universal time variations. *Journal of Geophysical Research*, *71*(3), 785–801. https://doi.org/10.1029/JZ071i003p00785

de Gasperin, F., Mevius, M., Rafferty, D. A., Intema, H. T., & Fallows, R. A. (2018). The effect of the ionosphere on ultra-low-frequency radio-interferometric observations. *Astronomy & Astrophysics*, *615*, A179. https://doi.org/10.1051/0004-6361/201833012

de Gasperin, F., Vink, J., McKean, J. P., Asgekar, A., Avruch, I., Bentum, M. J., et al. (2020). Cassiopeia A, Cygnus A Taurus A, and Virgo A at ultra-low radio frequencies. *Astronomy & Astrophysics*, *635*, A150. https://doi.org/10.1051/0004-6361/201936844

Doan, J. W., & Forsyth, P. A. (1978). Mid-latitude quasi-periodic scintillations of satellite beacon signals. *Journal of Atmospheric and Terrestrial Physics*, *40*(9), 981–990. 0021-9169/78/0901-0981. https://doi.org/10.1016/0021-9169(78)90001-6

Dorrian, G. D., Breen, A. R., Davies, J. A., Rouillard, A. P., Fallows, R. A., Whittaker, I. C., et al. (2010). Transient structures and stream interaction regions in the solar wind: Results from EISCAT interplanetary scintillation, STEREO HI and *Venus Express* ASPERA-4 Measurements. *Solar Physics*, *265*(1–2), 207–231. https://doi.org/10.1007/s11207-010-9599-z

Dorrian, G. D., Fallows, R., Wood, A., Themens, D. R., Boyde, B., Krankowski, A., et al. (2023). LOFAR observations of substructure within a traveling ionospheric disturbance at mid-latitude. *Space Weather*, *21*(1), e2022SW003198. https://doi.org/10.1029/2022SW003198

Elkins, J., & Slack, F. F. (1969). Observations of travelling ionospheric disturbances using stationary satellites. *Journal of Atmospheric and Terrestrial Physics*, *31*(3), 421–439. https://doi.org/10.1016/0021-9169(69)90067-1

Fallows, R. A., Bisi, M. M., Forte, B., Ulich, T., Konovalenko, V. V., Mann, G., & Vocks, C. (2016). Separating nightside interplanetary and ionospheric scintillation with LOFAR. *The Astrophysical Journal Letters*, *828*(1), L7. https://doi.org/10.3847/2041-8205/828/1/L7

Fallows, R. A., Coles, W. A., McKay-Bukowski, D., Vierinen, J., Virtanen, I. I., Postila, M., et al. (2015). Broadband meter-wavelength observations of ionospheric scintillation. *Journal of Geophysical Research: Space Physics*, *119*(12), 10544–10560. https://doi.org/10.1002/2014JA020406

Fallows, R. A., Forte, B., Astin, I., Allbrook, T., Arnold, A., Wood, A., et al. (2020). A LOFAR observation of ionospheric scintillation from two simultaneous travelling ionospheric disturbances. *Journal of Space Weather and Space Climate*, *10*, 10. https://doi.org/10.1051/swsc/2020010

From, W. R., & Whitehead, J. D. (1986). E_s structure using an HF radar. *Radio Science*, *21*(3), 309–312. https://doi.org/10.1029/RS021i003p00309

Hocke, K., & Igarashi, K. (2003). Wave-optical simulation of the oblique HF radio field. *Radio Science*, *38*(3), 1039. https://doi.org/10.1029/2002RS002691

Hunsucker, R. D. (1982). Atmospheric gravity waves generated in the high-latitude ionosphere: A review. *Reviews of Geophysics*, *20*(2), 293–315. https://doi.org/10.1029/RG020i002p00293

Hysell, D. L., Munk, J., & McCarrick, M. (2014). Sporadic *E* ionization layers observed with radar imaging and ionospheric modification. *Geophysical Research Letters*, *41*(20), 6987–6993. https://doi.org/10.1002/2014GL061691

Iyemori, T. (1990). Storm-time magnetospheric currents inferred from mid-latitude geomagnetic field variations. *Journal of Geomagnetism and Geoelectricity*, *42*(11), 1249–1265. https://doi.org/10.5636/jgg.42.1249

Jiang, C., Yang, G., Liu, J., Yokoyama, T., Komolmis, T., Song, H., et al. (2016). Ionosonde observations of daytime spread *F* at low latitudes. *Journal of Geophysical Research: Space Physics*, *121*(12), 12093–12103. https://doi.org/10.1002/2016JA023123

Kelley, M. C., & Ilma, R. R. (2016). Generation of a severe convective ionospheric storm under stable Rayleigh-Taylor conditions: Triggering by meteors? *Annales Geophysicae*, *34*(2), 165–170. https://doi.org/10.5194/angeo-34-165-2016

Kintner, P. M., Ledvina, B. M., & de Paula, E. R. (2005). An amplitude scintillation test pattern standard for evaluating GPS receiver performance. *Space Weather*, *3*, S03002. https://doi.org/10.1029/2003SW000025

Kintner, P. M., Ledvina, B. M., & de Paula, E. R. (2007). GPS and ionospheric scintillations. *Space Weather*, *5*(9), S09003. https://doi.org/10.1029/2006SW000260

Main, R. A., Parthasarathy, A., Johnston, S., Karastergiou, A., Basu, A., Cameron, A. D., et al. (2023). The Thousand Pulsar Array programme on MeerKAT – X. Scintillation arcs of 107 pulsars. *Monthly Notices of the Royal Astronomical Society*, *518*(1), 1086–1097. https://doi.org/10.1093/mnras/stac3149

Mall, G., Main, R. A., Antoniadis, J., Bassa, C. G., Burgay, M., Chen, S., et al. (2022). Modelling annual scintillation arc variations in PSR J1643−1224 using the Large European Array for Pulsars. *Monthly Notices of the Royal Astronomical Society*, *511*(1), 1104–1114. https://doi.org/10.1093/mnras/stac096

Maruyama, T. (1991). Observations of quasi-periodic scintillations and their possible relation to the dynamics of E_s plasma blobs. *Radio Science*, *26*(3), 691–700. https://doi.org/10.1029/91RS00357

Maruyama, T. (1995). Shapes of irregularities in the sporadic *E* layer producing quasi-periodic scintillations. *Radio Science*, *30*(3), 581–590. https://doi.org/10.1029/95RS00830

Maruyama, T., Fukao, S., & Yamamoto, M. (2000). A possible mechanism for echo striation generation of radar backscatter from midlatitude sporadic *E*. *Radio Science*, *35*(5), 1155–1164. https://doi.org/10.1029/1999RS002296

Mevius, M., van der Tol, S., Pandey, V. N., Vedantham, H. K., Brentjens, M. A., de Bruyn, A. G., et al. (2016). Probing ionospheric structures using the LOFAR radio telescope. *Radio Science*, *51*(7), 927–941. https://doi.org/10.1002/2016RS006028

Meyer-Vernet, N. (1980). On a day-time ionospheric effect on some radio intensity measurements and interferometry. *Astronomy & Astrophysics*, *84*, 142–147. Retrieved from https://ui.adsabs.harvard.edu/abs/1980A&A…84…142M

Moskaleva, E. V., & Zaalov, N. Y. (2013). Signature of polar cap inhomogeneities in vertical sounding data. *Radio Science*, *48*(5), 547–563. https://doi.org/10.1002/rds.20060

Oppenheim, M. M., & Dimant, Y. (2006). Meteor induced ridge and trough formation and the structuring of the nighttime E-region ionosphere. *Geophysical Research Letters*, *33*(24), L24105. https://doi.org/10.1029/2006GL028267

Patel, K., Singh, A. K., Singh, A. K., & Singh, R. P. (2009). Characteristics of quasi-periodic scintillations observed at low latitude. *Radio Science*, *44*(6), RS6007. https://doi.org/10.1029/2008RS003975

Rao, J., Ren, R., Chen, H., Yu, Y., & Zhou, Y. (2018). The stratospheric sudden warming event in February 2018 and its prediction by a climate system model. *Journal of Geophysical Research: Atmospheres*, *123*(23), 13332–13345. https://doi.org/10.1029/2018JD028908

Renkwitz, T., Sivakandan, M., Jaen, J., & Singer, W. (2023). Ground-based noontime D-region electron density climatology over northern Norway. *Atmospheric Chemistry and Physics*, *23*(19), 10823–10834. https://doi.org/10.5194/acp-23-10823-2023

Saito, S., Yamamoto, M., Hashiguchi, H., & Maegawa, A. (2006). Observation of three-dimensional structures of quasi-periodic echoes associated with mid-latitude sporadic-E layers by MU radar ultra-multi-channel system. *Geophysical Research Letters*, *33*(14), L14109. https://doi.org/10.1029/2005GL025526

Snively, J. B., & Pasko, V. P. (2003). Breaking of thunderstorm-generated gravity waves as a source of short-period ducted waves at mesopause altitudes. *Geophysical Research Letters*, *30*(24), 2254. https://doi.org/10.1029/2003GL018436

Sokolovskiy, S. V. (2001). Modeling and inverting radio occultation signals in the moist troposphere. *Radio Science*, *36*(3), 441–458. https://doi.org/10.1029/1999RS002273

Song, K., Meziane, K., Kashcheyev, A., & Jayachandran, P. T. (2022). Multifrequency observation of high latitude scintillation: A comparison with the phase screen model. *IEEE Transactions on Geoscience and Remote Sensing*, *60*, 1–9. https://doi.org/10.1109/TGRS.2021.3113778

Stinebring, D. R., McLaughlin, M. A., Cordes, J. M., Becker, K. M., Goodman, J. E. E., Kramer, M. A., et al. (2001). Faint scattering around pulsars: Probing the interstellar medium on solar system size scales. *The Astrophysical Journal*, *549*(1), L97–L100. https://doi.org/10.1086/319133

van Haarlem, M. P., Wise, M. W., Gunst, A. W., Heald, G., McKean, J. P., Hessels, J. W. T., et al. (2013). LOFAR: Low-frequency-array. *Astronomy and Astrophysics*, *556*, A2. https://doi.org/10.1051/0004-6361/201220873

Vruno, F. D., Winkel, B., Bassa, C. G., Józsa, G. I. G., Brentjens, M. A., Jessner, A., & Garrington, S. (2023). Unintended electromagnetic radiation from Starlink satellites detected with LOFAR between 110 and 188 MHz. *Astronomy and Astrophysics*, *676*(20), A75. https://doi.org/10.1051/0004-6361/202346374

Walker, M. A., Koopmans, L. V. E., Stinebring, D. R., & van Straten, W. (2008). Interstellar holography. *Monthly Notices of the Royal Astronomical Society*, *388*(3), 1214–1222. https://doi.org/10.1111/j.1365-2966.2008.13452.x

Welch, P. (1967). The use of fast Fourier transform for the estimation of power spectra: A method based on time averaging over short, modified periodograms. *IEEE Transactions on Audio and Electroacoustics*, *15*(2), 70–73. https://doi.org/10.1109/TAU.1967.1161901

Woodman, R. F., Yamamoto, M., & Fukao, S. (1991). Gravity wave modulation of gradient drift instabilities in mid-latitude sporadic *E* irregularities. *Geophysical Research Letters*, *18*(7), 1197–1200. https://doi.org/10.1029/91GL0115

Yamamoto, M., Fukao, S., Ogawa, T., Tsuda, T., & Kato, S. (1992). A morphological study on mid-latitude E-region field-aligned irregularities observed with the MU radar. *Journal of Atmospheric and Terrestrial Physics*, *54*(6), 769–777. ISSN 0021-9169. https://doi.org/10.1016/0021-9169(92)90115-2

Yamamoto, M., Fukao, S., Woodman, R. F., Ogawa, T., Tsuda, T., & Kato, S. (1991). Mid-latitude *E* region field-aligned irregularities observed with the MU radar. *Journal of Geophysical Research*, *96*(A9), 15943–15949. https://doi.org/10.1029/91JA01321